ELSEVIER

Contents lists available at ScienceDirect

International Journal of Mechanical Sciences

journal homepage: www.elsevier.com/locate/ijmecsci



Pervasive cracking of heterogeneous brittle materials using a multi-directional smeared crack band model*



Alden C. Cook^a, Senthil S. Vel^{a,*}, Scott E. Johnson^b

- ^a Department of Mechanical Engineering, University of Maine, Orono, Maine 04469, USA
- b School of Earth and Climate Sciences, University of Maine, Orono, Maine 04469, USA

ARTICLE INFO

Keywords: Smeared crack band Sequentially linear analysis Multi-directional crack Pervasive cracking Heterogeneous material Anisotropy Polycrystalline material

ABSTRACT

A numerical methodology is presented for the plane stress analysis of pervasive cracking in heterogeneous materials. The smeared crack band concept is used in conjunction with the multi-directional crack model to objectively model cracking in a finite element analysis while allowing cracks to form at different orientations. The multi-directional crack approach is able to reduce stress-locking behavior that plagues conventional fixed crack models. An advanced meshing technique is used to generate meshes with smooth grain boundaries and high-quality elements of uniform size. The sequentially linear analysis procedure is used in place of an iterative method to avoid instability issues and to capture the snap-type behavior of brittle materials. The implementation is generalized to allow for the analyses of heterogeneous materials composed of anisotropic constituents; furthermore, elastic stiffnesses and fracture parameters of the materials studied can vary with orientation. The proposed methodology is used to study cracking in a concrete microstructure obtained using X-ray computed tomography. Bulk constitutive behavior and crack patterns are compared with results of other crack methods in the literature. The proposed methodology is also used to analyze cracking within a computer-generated polycrystalline microstructure composed of Voronoi-like grains with the properties of alumina. Using the capabilities of the proposed methodology, a comparative study is performed by varying the tensile strengths along grain boundaries relative to their interiors.

© 2017 Elsevier Ltd. All rights reserved.

1. Introduction

Cracking in a heterogeneous material depends upon many factors including the phase morphology, the generally anisotropic elastic stiffnesses, strengths and fracture toughnesses of the constituent phases, and the behavior of grain boundaries. In many cases, finite element (FE) analysis is used in conjunction with a cracking model to simulate progressive cracking caused by a set of applied loads. Accuracy of the FE results generally requires specialized meshing techniques which, based on the cracking model, appropriately discretize individual grains and their respective boundaries.

Significant advances in crack modeling have been made over the last several decades. Many of the constitutive frameworks developed during this time were inspired by the cohesive zone model [1,2]. Examples include the discrete crack [3,4] and smeared [5–7] crack band approaches, which found widespread use in a number of applications [e.g. 7,8,9,10,11–13,14]. The smeared crack band concept is generally simpler to implement since, as opposed to the discrete concept, the topology of the finite element mesh remains unchanged during a

cracking simulation. Both approaches are available within most commercial finite element packages. Conventional FE analyses incorporating the classical discrete crack or smeared crack band framework typically suffer from directional mesh bias, i.e., strains tend to localize along continuous mesh lines due to the structure and geometry of the mesh. More recently, crack tracking algorithms have been incorporated into these models to reduce directional mesh bias [e.g. 15,16,17].

For cracking models which are based on fracture mechanics [18] or the cohesive zone model [1,2,19], material properties such as elastic stiffnesses, tensile strength, and fracture energy are typically needed for each phase. In addition, constitutive frameworks such as the discrete and smeared crack concepts may require a traction (stress) - displacement (strain) law and/or the material characteristic length [6] for each phase. Depending on the type of analysis, additional information may be necessary to define behavior along grain boundaries. For many anisotropic materials, elastic stiffnesses can be readily found in the literature; however, there is insufficient experimental data for the direction-dependent fracture properties of anisotropic materials. Until more data is collected, assumptions and/or approximations are necessary to study cracking in

E-mail addresses: alden.cook@gmail.com (A.C. Cook), senthil.vel@maine.edu (S.S. Vel).

^{*} Corresponding author.

anisotropic materials. That being said, much knowledge can be gained from studies which consider the influence of other analysis variables such as finite element size and type [e.g. 20] and applied loading conditions [e.g. 12].

Other numerical procedures have recently been developed which insert discontinuities directly into the element kinematics. This class of numerical methods includes the extended finite element method (XFEM) [e.g. 21,22,23] and the embedded crack models (EFEM) [e.g. 24,25,26,27]. Initial implementations of XFEM assumed stress-free cracks; later studies improved the method by incorporating cohesive cracks [28,29]. Element and nodal enrichments allow for the formation of arbitrarily oriented discontinuities, circumventing the meshing requirement of some discrete crack models. However, crack tracking algorithms are still necessary to determine the correct elements/nodes to enrich; in fact, EFEM without crack tracking has displayed directional mesh bias similar to the classical smeared crack concept [30]. Models employing XFEM and EFEM strategies are becoming increasingly popular due to the promising results obtained thus far. As stated in [20], most applications focus on simpler models which consider materials such as plain concrete, and more validation studies must be performed; that being said, progress towards more complicated models is being made [e.g. 31,32].

Now that mapping techniques such as electron backscatter diffraction and x-ray computed tomography provide microscopic maps of materials, meso/microscale modeling of cracking in heterogeneous materials is becoming increasingly popular [e.g. 33,34,35]. There is a growing demand for the development of micromechanical models which can help to better understand failure mechanisms, beginning at the scale of individual grains and constituent phases. Given the general complexity involved in an analysis of heterogeneous materials at the level of the meso/microstructure, models must be straightforward, robust, and efficient. Despite the apparent need for such models, many studies remain focused on simpler problems such as cracking in homogeneous, isotropic materials [12,20,36]. As an indirect result, there appears to be less demand for experimental data on fracture properties of anisotropic materials [33], and the few models which consider more complex material behavior lack sufficient options for the validation of results, e.g., crack patterns and bulk load(stress)-displacement(strain) relations.

In order to advance the understanding of cracking at the scale of individual constituents in heterogeneous materials, a generalized methodology has been developed which combines the multi-directional smeared crack band approach and the sequentially linear analysis (SLA) method within a standard FE framework. The implementation is capable of objectively studying pervasive cracking in heterogeneous materials while at the same time limiting stress-locking that would otherwise occur in single-fixed or orthogonal-fixed crack models. Stress locking has been extensively studied by Zimmermann and Jirasek [37] and is believed to arise from a finite element's inability to appropriately represent, in a smeared fashion, a discontinuity and the cohesive laws by which it is governed. The multi-directional crack approach is employed here as a means to reduce stress locking and thereby more accurately represent the cohesive relations which would exist between the two interfaces of a discrete crack. In addition, the current methodology has been generalized to allow for anisotropic material properties (if the experimental data exist) such as anisotropic stiffnesses, tensile strengths, and fracture energies. Within the multi-directional crack framework, this allows for element crack planes that each have a unique sets of material properties. In addition, the properties of specific crack planes within elements along grain/phase boundaries can be modified to model the presence of weaker regions in materials such as interface transition zones. Unlike certain discrete crack models which require frequent modification of the mesh connectivity, the topology of a mesh in the current work remains the same throughout an analysis, i.e., it is not necessary to detach nodes and/or re-mesh. From a conceptual standpoint, discrete cracks are seen as more physically representative of natural cracks which develop in materials on a local level. Smeared cracks, on the other hand, appear to

better represent distributed cracking in materials with relatively large fracture process zones such as concrete and rocks [38]. In distributed cracking, a smeared crack is used to represent a macroscopic crack which forms due to the coalescence of many individual local cracks. For the analysis of localized cracking, use of the smeared crack approach is relatively new and untested; however, smeared cracking can greatly simplify FE analysis by removing the need to re-mesh and by allowing cracks to form in arbitrary directions [e.g. 39]. One of the arguments which questions the use of the smeared approach in localized cracking is the difficulty in approximating thin, discrete cracks over the width of finite elements. The approximation can be improved by sufficiently reducing the size of finite elements a priori, along with the appropriate adjustments to the material softening laws through the crack band model [6]. Both the discrete crack approach and iterative schemes such as Newton-Raphson can suffer from instability issues when modeling brittle material behavior. Since the proposed model incorporates the SLA method, snap-type cracking behavior of brittle materials can be captured directly without numerical hindrance. In addition, the SLA implementation avoids conditioning issues encountered when working with negative tangent stiffnesses by using sets of reduced secant stiffnesses, i.e., unloading/reloading properties. Finally, the numerical implementations of the meshing routine and the analysis framework are efficient, stable, steady, conceptually straightforward, and require relatively few user input parameters. To our knowledge, there exists no other study which combines the smeared crack band concept, the multi-directional crack model, and the SLA method within an FE framework for the analysis of heterogeneous materials composed of generally anisotropic phases.

In Section 2.1, differences between the classical discrete and smeared crack concepts are discussed. Subsequently, the crack band approach of Bazant and Oh [6] is described, followed by the conventional formulations of the multi-directional crack approach and the SLA method. Aspects of the numerical implementation of the proposed methodology are conveyed, and validation studies are performed to ensure that element size sensitivity and directional mesh bias have been mitigated. After validation, the methodology is illustrated by considering two model problems. In the first problem, analysis of tensile cracking behavior of the two-dimensional concrete specimen of Ren et al. [33] is performed. Results for an applied vertical uniaxial load are compared with those presented by Ren et al. [33]. In the second problem, crack development in a Voronoi-like computer-generated polycrystalline microstructure is studied. Each anisotropic grain within the microstructure is assigned a random crystallographic orientation to introduce heterogeneity in elastic stiffnesses among the grains. Certain potential crack planes in grain boundary elements are given weaker properties to represent interface transition zones. Bulk behavior and crack development for different reductions in grain boundary strength are compared between three different analyses.

2. Background

The model developed here for the study of localized cracking in heterogeneous materials combines a number of different strategies that have been used to analyze brittle and quasi-brittle behavior in concrete and rocks. In this section, the fundamental details pertaining to discrete and smeared crack concepts, the crack band approach, the multi-directional crack model, and the SLA procedure are recapitulated.

2.1. Smeared crack modeling

Discrete and smeared crack concepts have been the subjects of debate for many years. As explained by Rots and Blaauwendraad [38], the discrete crack concept typically aligns with our intuition in terms of conceiving an actual geometric discontinuity between two fully detached crack interfaces; on the other hand, bands of localized cracks in materials such as concrete have been more easily modeled using smeared crack representations. Furthermore, instabilities created by the stiff interface

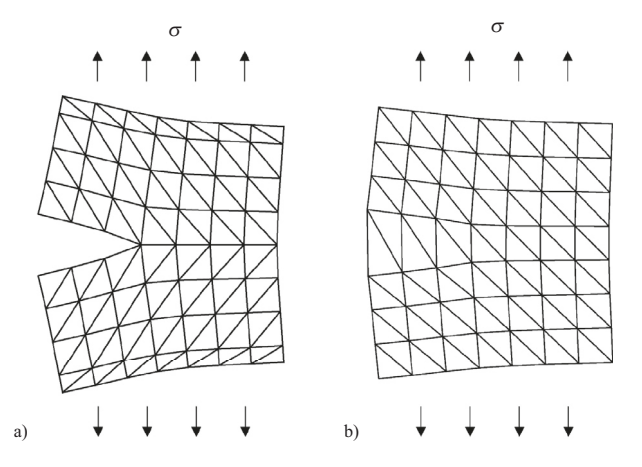


Fig. 1. Classical crack concepts. The deformed shapes are shown for an applied uniform reference load on the top and bottom surfaces. (a) Discrete cracking approach and (b) smeared cracking approach.

elements used in discrete modeling suggest that the smeared crack approach is better at representing early stages of distributed cracking. To exploit the advantages of both approaches, studies have considered combining discontinuous and continuous FE methods [e.g. 40].

In the smeared crack approach introduced by Rashid [5], the development of a crack is modeled by adjusting the constitutive properties, i.e., stiffnesses and strength, of conventional finite elements (see Fig. 1b). Once a smeared crack is fully developed, the displacements within the mesh remain continuous, producing strains which are still defined but are generally large within the element. Initial applications of the smeared crack approach aimed to describe large areas of distributed cracking in quasi-brittle materials such as concrete, and in this sense the approach was limited to global analyses of large-scale structures [5].

Despite the utility of discrete and smeared crack concepts in the numerical modeling of strain localization, both suffer from mesh dependency, i.e., the characteristics of the FE spatial discretization influence results such as bulk load-displacement curves and crack patterns. Sensitivity to the mesh is typically displayed in two forms: (1) sensitivity to the size of elements, and (2) sensitivity to the structure of the mesh, as well as the orientation and organization of its elements. Herein, the former is referred to as element size sensitivity and the latter is referred to as directional mesh bias. In smeared crack analyses, the detrimental effects of both element size sensitivity and directional mesh bias are apparent when strains localize into the smallest possible bands of elements that reside along continuous mesh lines. Detailed studies of mesh sensitivity have been performed to determine the influence of finite element type, size, and orientation [e.g. 20,41]. In efforts to reduce element size sensitivity and directional mesh bias in smeared crack analyses, researchers have incorporated the crack band model (see Section 2.2) and - crack tracking algorithms (see Section 3.2), respectively.

2.2. Crack band model

In early applications of the smeared crack concept, energy dissipated due to cracking depended on the size of finite elements. This issue was corrected by Bazant and Oh [6] upon introduction of the crack band model for general strain-softening materials. Today, the smeared crack concept and crack band model are collectively referred to as the smeared crack band approach. In order to mitigate mesh size dependence, the slope of the softening portion of the stress-strain curve is adjusted in order to ensure that the correct amount of fracture energy G_f is dissipated during the fracture process. This is achieved by linking the slope of the softening curve to a crack band width l_c which is related to the size and type of the finite element over which the cracking is distributed (see Section 3.1). In the case of linear softening under tension, the softening

slope E_t of the uniaxial stress-strain curve is adjusted according to

$$E_{t} = \left(\frac{1}{E} - \frac{2G_{f}}{f_{t}^{2} l_{c}}\right)^{-1},\tag{1}$$

where E is the Young's modulus in the direction normal to the crack and f_t is the corresponding tensile strength. Adjustment of the softening slope E_t results in an adjusted ultimate strain ε_{ult} given by

$$\varepsilon_{ult} = \frac{2G_f}{f_t l_c}. (2)$$

Bazant and Oh [6] showed that a restriction must be imposed on the maximum value of l_c to avoid local "snap-back" behavior:

$$l_c < \frac{2G_f E}{f_c^2},\tag{3}$$

where equality of both sides in the above equation results in a sudden stress drop normal to the crack.

A prominent feature of the smeared crack band model when applied to initially isotropic materials is the transition to an orthotropic elastic stiffness matrix at the onset of crack initiation. The transition results from the imposed degradation of material properties such as Young's modulus in the direction normal to the developing crack surface. Early studies using the smeared crack band approach defined a priori the fixed orientations in which cracks could form [6]. Later studies removed this restriction by allowing cracks to form normal to the maximum principal stress directions [39], after which the crack orientation was fixed for the remainder of the simulation. Further capabilities were added to the smeared crack band model to handle cases of multiaxial loading by allowing for the existence of a second fixed crack plane normal to the first [e.g. 20].

Despite their utility, fixed crack models are generally plagued by stress locking, an inherent deficiency encountered when modeling discontinuities as continuous fields over finite elements. Stress locking prevents elements from representing fully developed cracks, and therefore impedes correct separation behavior along crack interfaces [42]. In addition, fixed crack models poorly represent cracking if principal stress and/or strain directions change during a simulation.

2.3. Multi-Directional crack model

An alternative approach to the fixed crack model described in the previous section was developed by De Borst and Nauta [7] to allow any number of cracks to form at arbitrary orientations to one another (see Fig. 2). This method, referred to as the multi-directional fixed crack method [38], allowed a new fixed crack to form whenever the normal stress along a plane exceeded the corresponding tensile strength; as a result, issues associated with stress locking and principal direction rotation were reduced. Early applications of the multi-directional fixed crack model limited the number of potential cracks at a given point by requiring a minimum separation angle between neighboring crack planes [38]. This restriction was enforced to prevent cracks from forming arbitrarily close to one another, but also to work within the limitations of computer memory at the time. Computers today have sufficient memory to study cases involving the formation of many crack planes.

The foundation of the multi-directional fixed crack model lies is the decomposition of the total strain vector $\boldsymbol{\varepsilon} = \left\{ \boldsymbol{\varepsilon}_1 \quad \boldsymbol{\varepsilon}_2 \quad \boldsymbol{\varepsilon}_3 \right\}^T$ into an elastic part $\boldsymbol{\varepsilon}^{el}$ and a crack part $\boldsymbol{\varepsilon}^{cr}$ according to

$$\varepsilon = \varepsilon^{el} + \varepsilon^{cr},\tag{4}$$

where strain vectors ϵ , ϵ^{el} , and ϵ^{cr} are defined within a global xy coordinate system. The strain decomposition can be visualized by imagining a material element composed of a set of developing cracks distributed

¹ Although the cracks in our two-dimensional analyses are modeled as lines, we refer to them as planes within this work in accordance with the literature.

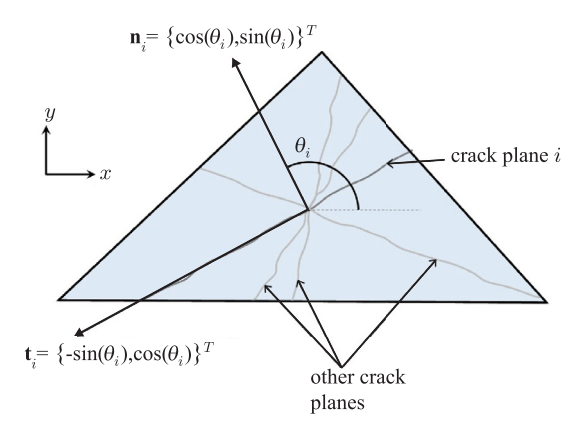


Fig. 2. Characteristics of the multi-directional crack model.

throughout an interconnected network of undamaged material. As can be seen from Eq. (4), the intact material characterized by global elastic strain ϵ^{el} acts like a spring in series with the cracking material characterized by global crack strain ϵ^{cr} . A global stress vector σ can also be defined as

$$\mathbf{\sigma} = \begin{pmatrix} \sigma_1 & \sigma_2 & \sigma_3 \end{pmatrix}^T. \tag{5}$$

The main advantage of strain decomposition is that the global crack strain ϵ^{cr} can be sub-decomposed into separate contributions from a number of non-orthogonal cracks that coexist at a material point

$$\boldsymbol{\varepsilon}^{cr} = \boldsymbol{\varepsilon}_1^{cr} + \boldsymbol{\varepsilon}_2^{cr} + \dots, \tag{6}$$

where global crack strain ε_i^{cr} is the contribution from crack i to the total global crack strain ε^{cr} . For crack plane i, an nt coordinate system can be defined in which the n-axis is aligned with the normal \mathbf{n}_i to the crack plane. The t-axis is then aligned with the vector \mathbf{t}_i parallel to the crack plane i (see Fig. 2). The local crack strain vector \mathbf{e}_i^{cr} for crack plane i in the nt coordinate system has components

$$\mathbf{e}_{i}^{cr} = \left\{ \varepsilon_{n,i}^{cr}, \gamma_{nt,i}^{cr} \right\}^{T}. \tag{7}$$

Likewise, a local stress vector \mathbf{s}_i for crack plane i can be defined in the nt coordinate system with components

$$\mathbf{s}_{i} = \left\{ \sigma_{n:i}, \tau_{nt:i} \right\}^{T}. \tag{8}$$

In order to relate the global stresses and crack strains in the xy coordinate system to the local stresses and crack strains in the nt coordinate system, the local stress and crack strain vectors are assembled into matrices \mathbf{s} and \mathbf{e}^{cr} of the form

$$\mathbf{s} = \begin{bmatrix} \mathbf{s}_1 & \mathbf{s}_2 & \dots \end{bmatrix}^T, \tag{9}$$

$$\mathbf{e}^{cr} = \begin{bmatrix} \mathbf{e}_1^{cr} & \mathbf{e}_2^{cr} & \dots \end{bmatrix}^T. \tag{10}$$

For a single crack i, the relation between the global crack strain and the local crack strain is given by

$$\boldsymbol{\varepsilon}_{i}^{cr} = \mathbf{N}_{i} \mathbf{e}_{i}^{cr}, \tag{11}$$

where the transformation matrix \mathbf{N}_i is composed of the components of crack plane unit normal vector $\mathbf{n}_i = \left\{\cos(\theta_i), \sin(\theta_i)\right\}^T$ and unit tangent vector $\mathbf{t}_i = \left\{-\sin(\theta_i), \cos(\theta_i)\right\}^T$, and has the form

$$\mathbf{N_i} = \begin{bmatrix} \cos^2(\theta_i) & -\cos(\theta_i)\sin(\theta_i) \\ \sin^2(\theta_i) & \cos(\theta_i)\sin(\theta_i) \\ 2\cos(\theta_i)\sin(\theta_i) & \cos^2(\theta_i)-\sin^2(\theta_i) \end{bmatrix}, \tag{12}$$

where θ_i is the angle between crack plane i and the global x-axis (see Fig. 2). Similar to Eqs. (9) and (10), the transformation matrices \mathbf{N}_i for each crack can be assembled as

$$\mathbf{N} = \begin{bmatrix} \mathbf{N}_1 & \mathbf{N}_2 & \dots \end{bmatrix}. \tag{13}$$

Repeated substitution of (11) into (6) yields the relation between the global crack strain vector ϵ^{cr} and the matrix \mathbf{e}^{cr} of assembled local crack strain vectors

$$\mathbf{\varepsilon}^{cr} = \mathbf{N}\mathbf{e}^{cr}.\tag{14}$$

Similarly, the global stress vector σ and the matrix ${\bf s}$ of assembled local stress vectors

$$\mathbf{s} = \mathbf{N}^T \mathbf{\sigma}. \tag{15}$$

Eqs. (14) and (15) can be used to derive the overall relation between global stress σ and global strain ε . First, it is noted that the global stress and the elastic part of the global strain are related through the constitutive equation

$$\mathbf{\sigma} = \mathbf{D}_0 \mathbf{\varepsilon}^{el},\tag{16}$$

where \mathbf{D}_0 is the undamaged element material stiffness matrix which for plane stress has the following general form for anisotropic materials

$$\mathbf{D}_{0} = \begin{bmatrix} D_{0;11} & D_{0;12} & D_{0;13} \\ D_{0;12} & D_{0;22} & D_{0;23} \\ D_{0;13} & D_{0;23} & D_{0;33} \end{bmatrix}. \tag{17}$$

The crack stress \mathbf{s}_i can be related to the crack strain \mathbf{e}_i^{cr} through constitutive matrix \mathbf{D}_i^{cr} according to

$$\mathbf{s}_i = \mathbf{D}_i^{cr} \mathbf{e}_i^{cr}. \tag{18}$$

Using (18), one may assemble the constitutive relations for each crack plane i according to

$$\mathbf{s} = \mathbf{D}^{cr} \mathbf{e}^{cr},\tag{19}$$

where \mathbf{D}^{cr} is an assemblage of 2×2 constitutive matrices relating the local stresses on crack planes to the local crack strains. Inserting the right hand side of (11) into (4) yields

$$\mathbf{\varepsilon} = \mathbf{\varepsilon}^{el} + \mathbf{N}\mathbf{e}^{cr}.\tag{20}$$

Combining (16) with (20) gives

$$\mathbf{\sigma} = \mathbf{D}_0(\mathbf{\varepsilon} - \mathbf{N}\mathbf{e}^{cr}),\tag{21}$$

which when premultiplied by \mathbf{N}^T and subsequently combined with (15) and (19) can be rearranged to give the local crack strain as a function of total global strain

$$\mathbf{e}^{cr} = \left[\mathbf{D}^{cr} + \mathbf{N}^T \mathbf{D}_0 \mathbf{N}\right]^{-1} \mathbf{N}^T \mathbf{D}_0 \mathbf{\epsilon}.$$
 (22)

Finally, the overall global stress-strain relation can be determined by inserting (22) into (21):

$$\mathbf{\sigma} = \left[\mathbf{D}_0 - \mathbf{D}_0 \mathbf{N} \left[\mathbf{D}^{cr} + \mathbf{N}^T \mathbf{D}_0 \mathbf{N} \right]^{-1} \mathbf{N}^T \mathbf{D}_0 \right] \mathbf{\epsilon}. \tag{23}$$

As shown in Eq. (23), the effective damaged stiffness matrix ${\bf D}$ is given by

$$\mathbf{D} = \mathbf{D}_0 - \mathbf{D}_0 \mathbf{N} [\mathbf{D}^{cr} + \mathbf{N}^T \mathbf{D}_0 \mathbf{N}]^{-1} \mathbf{N}^T \mathbf{D}_0.$$
 (24)

The damaged stiffness matrix \mathbf{D} is equal to the corresponding undamaged stiffness matrix \mathbf{D}_0 diminished by a matrix which accounts for the weakening effects of developed crack planes.

In general, the constitutive matrix \mathbf{D}_i^{cr} for crack plane i is a full matrix containing terms which relate each component of local stress \mathbf{s}_i to all components of local crack strain \mathbf{e}_i^{cr} . It is common, however, to ignore shear-normal coupling and assume that \mathbf{D}_i^{cr} is a diagonal matrix

$$\mathbf{D}_{i}^{cr} = \begin{bmatrix} D_{i}^{I} & 0\\ 0 & D_{i}^{II} \end{bmatrix}. \tag{25}$$

where D_i^I relates the local normal stress $\sigma_{n;i}$ to the local crack normal strain $\epsilon_{n;i}^{cr}$, and D_i^{II} relates the local shear stress $\tau_{n;i}$ to the local crack shear strain $\gamma_{nr;i}^{cr}$ [43].

For crack plane i, it is necessary to define unloading-reloading behavior. For example, in the case of secant unloading-reloading, the normal component D_i^I in constitutive matrix \mathbf{D}_i^{cr} can be expressed as

$$D_i^I = \frac{E_{0;i} E_i}{E_{0;i} - E_i},\tag{26}$$

where $E_{0;i}$ and E_i are the undamaged and secant Young's moduli in the direction normal to crack plane i, respectively [7]. This form can be derived from the decomposition of total normal stain into elastic normal strain and crack normal strain.

Fixed crack models typically require adjustment of the shear behavior in order to avoid the residual shear stresses which can occur along fully developed crack planes not aligned with the principal directions [20]. For tensile cracking, the shear component D_i^{II} has been approximated as a function of the normal strain [7,44] according to

$$D_i^{II} = \frac{\beta_i}{1 - \beta_i} G_i,\tag{27}$$

where G_i is the shear modulus determined from the stiffness matrix in the coordinate system of the i^{th} plane, and β_i is a reduction factor which is commonly taken as a function of the crack development in the normal direction. The assumed form for β_i used in this study will be described in Section 3.3.1.

2.4. Sequentially linear analysis

During an FE analysis, brittle, snap-type fracturing of materials such as ceramic, concrete, and rock can cause convergence issues when using iterative analysis methods such as the Newton–Raphson scheme. These issues typically present themselves as abrupt manifestations of geometric discontinuities and/or sudden variations in material properties. The sequentially linear analysis (SLA) method [20,36,45] was developed with the specific purpose of modeling such behavior by reproducing the discontinuous events typical of brittle and quasi-brittle materials. Unlike iterative methods which discretize the loads applied to a structure and assume smooth material stress-strain relations, SLA discretizes the damage through a set of predefined reductions in material strength and stiffness; consequently, SLA is defined as a non-iterative procedure.

The original SLA implementation typically consists of a series of scaled linear analyses within a single fixed crack modeling framework. During each analysis, a critical integration point is determined based on its current strength to principal stress ratio. The critical point is subsequently damaged in the maximum principal stress direction by a finite amount, resulting in a stepwise reduction of tensile strength and Young's modulus along a plane normal to the principal stress direction. After initial cracking has begun in an element, the orientation of the crack plane in that element is fixed for the remainder of the analysis. The amount by which strengths and Young's moduli are reduced is determined by a sawtooth curve approximating the uniaxial material softening relation. The sawtooth curve, composed of a set of sawteeth, defines the tensile strengths and Young's moduli of the material at different stages of crack development. Fig. 3 shows a typical sawtooth approximation of a linear softening curve.

In our work, we follow the approach of Slobbe [48] by employing the improved ripple approach to generate sawtooth approximations for material softening curves. Although we keep other aspects of the original SLA framework described in [20], we generalize the approach by allowing cracks to form within elements along a number of predefined fixed element crack planes. If cracking has not yet started along a given plane, it is referred to herein as a "potential" element crack plane. By defining an appropriate number of potential crack planes within all elements a priori, one can accurately capture the development and propagation of multiple cracks during the SLA procedure. More details pertaining to our generalized implementation of the SLA method are given in Sections 3.3 and 3.4. The reader should refer to [20] for details pertaining to the sawtooth approximation of material softening relations.

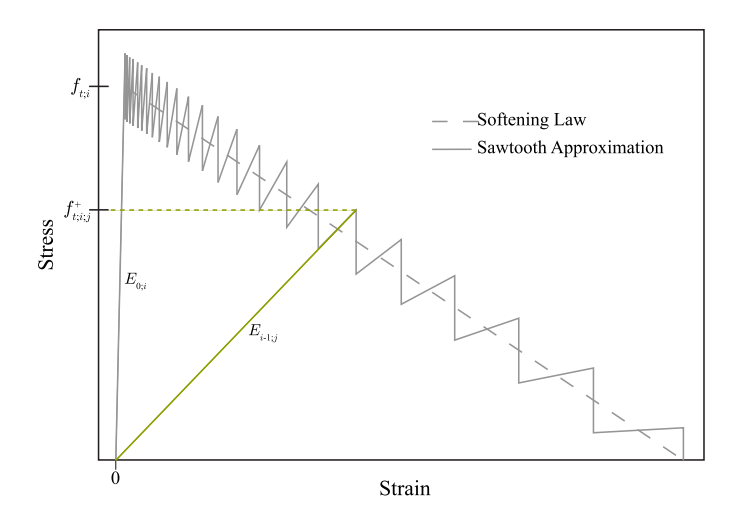


Fig. 3. Typical sawtooth approximation for the linear softening behavior of element crack plane i

3. Proposed methodology

In this section, a novel modeling strategy is described which has been designed for the purpose of studying objective, pervasive cracking in heterogeneous anisotropic materials. The approach described herein combines the smeared crack band model, the multi-directional fixed crack method, and the SLA procedure within a finite element framework. In this work, we employ a mesh generation process which was developed to discretize heterogeneous material microstructures derived from electron backscatter diffraction maps, X-ray computer tomography scans, or pixelated image data. The mesh generation process, which produces meshes composed of high-quality, uniformly-sized, triangular elements which conform to the phase/grain boundaries, has been thoroughly described in [46] and [47].

In Section 3.1, a description is provided regarding the process by which the crack band width $l_{c;i}$ is determined a priori for each potential crack plane i contained within an element of the FE mesh. As mentioned in Section 2.2, the crack band width $l_{c;i}$ ensures results which do not depend on element size. In Section 3.2, details are provided regarding an incorporated crack tracking algorithm which is shown to reduce the influence of mesh directional bias. The implementations of the crack band approach and the crack tracking algorithm are validated in Section 4.1 and Section 4.2, respectively. Section 3.3 outlines the method by which an element crack plane's elastic and fracture properties are degraded due to crack initiation or progression. Finally, the procedural aspects of our numerical implementation are given in Section 3.4.

3.1. Element crack plane band width

The crack band width l_c introduced in Section (2.2) can be thought of as an FE discretization parameter which adjusts the softening portion of the constitutive model to ensure objectivity of results with respect to element size [6]. As an FE discretization parameter, the crack band width l_c is a function of the element geometry and size. Accurate representation of the crack band width ensures correct energy dissipation during cracking and to some extent reduces mesh directional bias. For the analysis of homogeneous concrete within a single fixed crack framework, [20] extensively described various crack band width estimators for a variety of two-dimensional elements containing different numbers of integration points. In the current formulation, a simple orthographic projection method [48] is incorporated for a priori approximation of crack band widths for all potential crack planes within constant strain, three-noded, triangular finite elements. Conceptually, the projection method produces a crack band width which corresponds to the two-dimensional

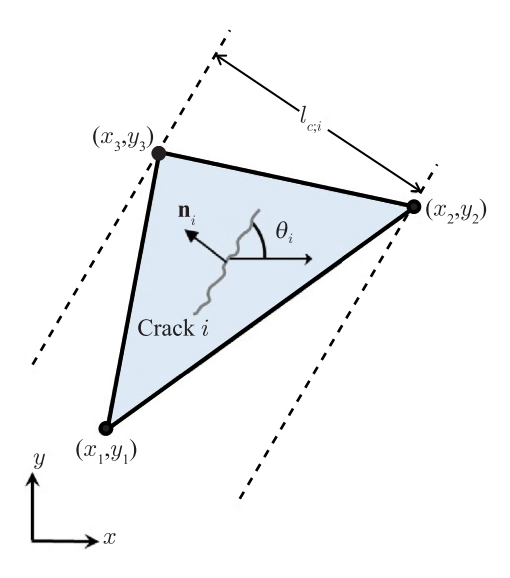


Fig. 4. Crack plane i in a typical triangular finite element.

element area projected onto a line perpendicular to the crack plane direction (see Fig. 4). Within the multi-directional crack framework, the crack band width $l_{c;i}$ of potential element crack plane i is a function of the orientation angle θ_i of the element crack plane relative to the element edges, and for polygonal elements, the value of $l_{c;i}$ is in general different for each potential crack plane.

The procedure for approximating the crack band width $l_{c;i}$ for potential element crack plane i is now described. The unit normal vector \mathbf{n}_i to an arbitrary element crack plane which makes an angle θ_i with the x axis is (see Fig. 4)

$$\mathbf{n_i} = \begin{cases} \cos(\theta_i) \\ \sin(\theta_i) \end{cases}. \tag{28}$$

Consider also the vectors created by the edges of the element to which the crack plane belongs

$$\mathbf{v}_{1} = \begin{cases} x_{2} - x_{1} \\ y_{2} - y_{1} \end{cases}, \quad \mathbf{v}_{2} = \begin{cases} x_{3} - x_{2} \\ y_{3} - y_{2} \end{cases}, \quad \mathbf{v}_{3} = \begin{cases} x_{1} - x_{3} \\ y_{1} - y_{3} \end{cases}, \tag{29}$$

where (x_j, y_j) are the xy coordinates of node j, and subscript k on vector \mathbf{v}_k denotes the vector for edge k. The crack band width $l_{c;i}$ for the element crack plane i is determined using (28) and (29) according to

$$l_{c;i} = \max(|\mathbf{n_i} \cdot \mathbf{v_1}|, |\mathbf{n_i} \cdot \mathbf{v_2}|, |\mathbf{n_i} \cdot \mathbf{v_3}|), \tag{30}$$

where $\mathbf{n_i} \cdot \mathbf{v_k}$ is the dot product between vectors $\mathbf{n_i}$ and $\mathbf{v_k}$.

Other methods for determining crack band widths have been developed for various two-dimensional element types [e.g. 9,44,49]. Comparisons between existing methods used to compute crack band widths have also been performed [9,20,50]. Furthermore, the estimation of the crack band width presented in [49] has been extended to three-dimensional problems [51]. The method employed in the current work is referred to as the standard projection method [50], and is equivalent to the method developed in [49] for constant strain triangular elements.

For multi-directional cracking, Rots and Blaauwendraad [38] assumed that the crack band width was the same for any crack plane which developed within an element. In the current work, this is generalized by allowing each plane to have a crack band width determined by (30). However, it is optimal to generate meshes which prevent significant variation of crack band widths between neighboring elements and an element's individual crack planes [20]. This can be achieved by producing meshes containing 1) elements of approximately the same area, i.e., uniformly-sized elements, and 2) elements whose edges are approximately the same length, i.e., high-quality elements. Consequently, heterogeneous morphologies with fine constituent features such as narrow regions or tapered sections require a sufficient number of elements

to maintain a uniform distribution of high-quality elements. Although we have not performed parametric studies based on mesh characteristics such as element size uniformity and element quality in this work, it has been suggested that superior results are expected in analyses using uniform meshes containing equilateral triangular elements [20].

3.2. Crack tracking algorithm

As described in Section 2.1, classical smeared crack band models suffer from strain localization along continuous mesh lines resulting from directional mesh bias. Existing studies have attempted to reduce the influence of directional mesh bias in smeared crack band models by incorporating crack tracking algorithms [e.g. 16,20]. In the current work, a crack tracking algorithm has been developed which, during any given scaled linear analysis within the SLA procedure, uses the existing crack history in conjunction with the orientation of the critical crack plane i_{crit} contained within the critical element e_{crit} to determine if a new crack has formed or if any of the existing cracks have propagated (see Section 3.4 for details pertaining to the implemented SLA method with crack tracking). The crack tracking algorithm developed here is similar to that proposed by Cervera et al. [16].

3.2.1. Definitions of elements in the crack tracking algorithm

During a scaled linear analysis in the SLA procedure, a critical element crack plane i_{crit} is selected by considering the normal stress on each element crack plane within all elements of the FE mesh. The element containing the critical crack plane is labeled as the critical element e_{crit} . For the purposes of the crack tracking algorithm, the critical element e_{crit} is defined as an isolated element, an intersected element, or a cracked element (see Fig. 5). In our implementation, an isolated element is always an element that has been user-defined prior to the beginning of the analysis as an element whose potential crack planes can initiate cracking without the element having any neighbors which contain existing crack planes. In other words, cracks always initiate in isolated elements. An intersected element is an element that does not yet contain an existing crack plane, i.e., all planes are still potential crack planes, but the element does share an edge with at least one other element that contains an existing crack plane. The potential crack planes within intersected elements are potential candidates for the propagation of existing cracks from neighboring cracked elements. A cracked element is any element that contains one or more existing crack planes; in other words, at least one crack plane in a cracked element has been selected as the critical crack plane i_{crit} in a previous scaled linear analysis.

3.2.2. Updating the crack tracking history

The crack tracking update procedure for each of the three types of elements introduced in Section 3.2.1 is now described. For a given scaled linear analysis in the SLA procedure, all existing and potential crack planes in cracked elements, as well as potential crack planes in intersected and isolated elements are considered when determining the new critical crack plane i_{crit} . Items introduced below are described visually in Fig. 5.

If i_{crit} is an existing crack plane which belongs to a cracked element, the SLA method proceeds by updating the stiffnesses and tensile strength in the direction normal to i_{crit} based on its sawtooth relation, and subsequently updating the properties of the critical element e_{crit} containing crack plane i_{crit} based on the update procedure that is described in Section 3.3. Since in this case e_{crit} is already classified as a cracked element, no new information is added to the crack tracking history, i.e., no neighboring elements become newly-defined intersected elements.

If i_{crit} is a potential crack plane which belongs to an intersected element, three items are determined: (1) two pairs of xy coordinates defining a line l which is parallel to critical crack plane i_{crit} , (2) the crack entry point p_{in} located along the element edge which is shared between e_{crit} and the neighboring cracked element, and (3) the exit point p_{out} determined as the point where one of the edges of element e_{crit} intersects line

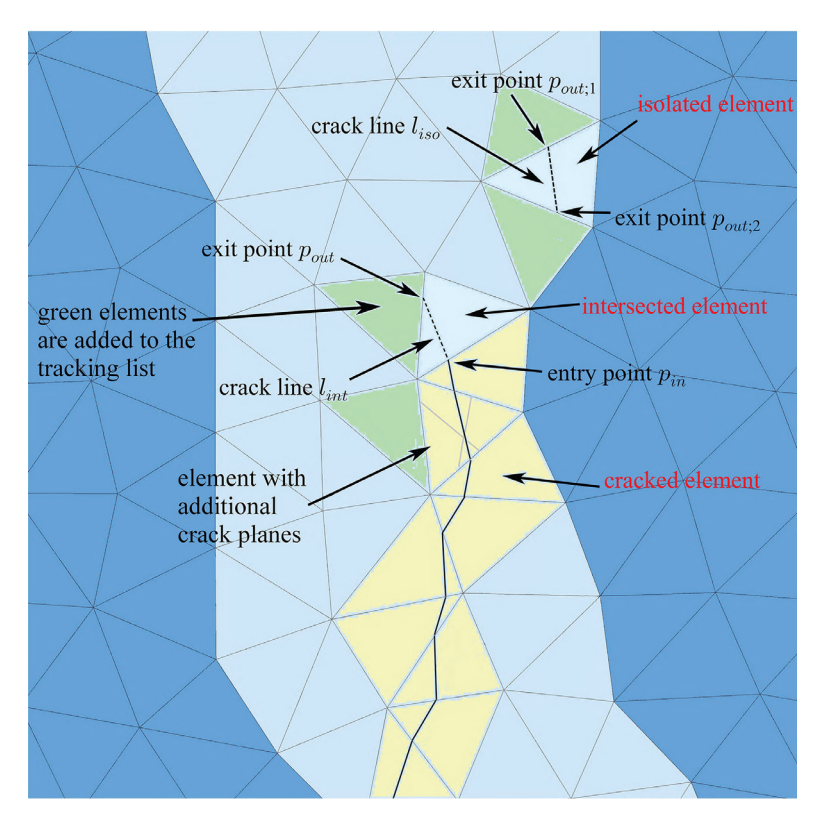


Fig. 5. Characterizations of elements in the crack tracking algorithm.

 $l_{\rm int}$, where $l_{\rm int}$ is created by moving one end of line l to entry point p_{in} without rotating l. The subscript "int" refers to the classification of the element as "intersected". As shown in Fig. 5, $l_{\rm int}$ is the new crack plane for the intersected element. The element neighboring e_{crit} which shares the edge intersected by $l_{\rm int}$ becomes an intersected element unless it is already defined as an intersected element or a cracked element. Element e_{crit} is removed from the list of intersected elements and is furthermore classified as a cracked element.

If critical plane i_{crit} belongs to an isolated element, three items are determined: (1) Line l which is determined in the same way as for an intersected element, (2) exit points $p_{out;1}$ and $p_{out;2}$ determined as the points where two of the edges of element e_{crit} intersect line l_{iso} , where l_{iso} is created by moving the center of line l to the centroid of element e_{crit} without rotation. The subscript "iso" refers to the classification of the element as "isolated". Each of the elements neighboring e_{crit} which shares an edge that is intersected by l_{iso} is classified as an intersected element, unless it is already an intersected element or a cracked element. Element e_{crit} is added to the list of cracked elements.

The crack tracking algorithm and the element definitions above can be better understood by outlining the progression of elements during the SLA procedure. Isolated elements, defined a priori by the user, initially contain only potential crack planes and become cracked elements if selected during a scaled linear analysis as e_{crit} . Intersected elements, sharing an edge with a cracked element, initially contain only potential crack planes and become cracked elements if selected during a scaled linear analysis as e_{crit} ; a neighboring unclassified element then becomes a new intersected element. Cracked elements, once defined, remain cracked elements for the duration of the SLA procedure. We note that certain crack propagation paths may end if the crack plane at the propagation front intersects an element edge that lies along a domain boundary. The crack tracking algorithm has the main purpose of eliminating directional mesh bias when single fixed cracks propagate from one element to another. In the multi-directional crack approach implemented here, multiple crack planes can develop within cracked elements. Allowing multiple crack planes to develop within a single element relieves stress-locking and helps to mitigate instances when initial crack directions are incorrect [e.g. 37]. If a secondary crack initiates in an element, the crack tracking restraints are relaxed in that element by allowing the remaining neighboring element, which is yet unclassified, to become a new pseudo isolated element. The adjective pseudo is used here since this isolated element is not user defined a priori but instead it is defined during an analysis to allow propagating element crack paths to branch and intersect with one another. In some cases, a newly cracked element, which was previously an intersected element, may contain an initial crack plane with an orientation that differs by more than 90 degrees from the previous cracked element with which it shares an edge containing the entrance point p_{in} . For homogeneous materials, this occurrence was studied by Cervera et al. [16] and is commonly known as crack reversal, or crack turn-around. Cervera et al. [16] mitigated this issue by preventing cracks from changing direction from one element to the next by a user-defined threshold angle. In our work, we do not use the crack reversal criteria in [16] since cracks could potentially change direction significantly along phase/grain boundaries in heterogeneous materials. Instead, we use the same approach as before for secondary cracking and classify other neighboring elements as pseudo isolated elements.

3.3. Updating crack plane properties

Since the multi-directional fixed crack model has been incorporated within the formulation, the current implementation of the SLA method proceeds slightly differently than the conventional implementation that was outlined in Section 2.4. In the next section, these differences are addressed by describing how the sawtooth method for approximating the softening behavior along element crack planes is employed. The process by which element crack plane properties, and thus element properties, are updated during the SLA method, is also described.

3.3.1. Defining sawtooth properties for multi-directional cracking

We describe the process by which sawtooth approximations of softening relations are generated by considering an arbitrary potential crack plane i within an element. Consider an arbitrary potential crack plane i located within an element composed of material with compliance matrix S_0 . The tensile strength $f_{t;i}$ and $G_{f;i}$ for the potential crack plane have been defined by the user based on knowledge of the material constitutive behavior, and the crack band width l_{ci} has been determined for the potential crack plane using methods from Section 3.1. In order to define the sawtooth approximation for the material softening behavior, we must determine the initial Young's modulus $E_{0:i}$ shear modulus $G_{0:i}$ in the directions normal and tangential to the potential crack plane, respectively. Using the in-plane orientation θ_i of potential crack plane i relative to the global x-axis, and the element's compliance matrix S_0 , one can determine both the initial Young's modulus $E_{0:i}$ and the shear modulus $G_{0:i}$ for the potential crack plane. Next, the improved ripple approach described by [20] can be used to generate a set of sawtooth properties for the potential crack plane. Using similar terminology to that presented in [20], the value of the Young's moduli and upper tensile strength at sawtooth j are defined as $E_{i,j}$ and $f_{t,i,j}^+$. Since we have employed the multi-directional crack approach, one can use the potential crack plane's initial Young's modulus E_{0} ; and the sawtooth Young's moduli $E_{i,j}$ to compute the corresponding sawtooth mode I moduli $D_{i,j}^I$ using Eq. (26). Recall that the mode I modulus relates the crack plane normal stress σ_n to the crack plane normal strain ε_n^{cr} according to Eqs. (18) and (25). As can be seen by considering (26), the initial mode I modulus value $D_{0:i}^{I}$ is infinite. In order to prevent numerical issues, $D_{0:i}^{I}$ can be set to a high, but finite value. In this work, the sawtooth mode II modulus $D_{i:j}^{II}$ is computed according to Eq. (27) with p=1, where β_i is defined as $E_{i;j}/E_{0;i}$. In this case, $D_{i:j}^{II}$ reduces proportionally with the Young's modulus $E_{i;j}$. In other studies, it has been proposed that modulus $D_{i:j}^{II}$ be determined from the crack plane normal strain ε_n^{cr} [e.g. 38,44]. However, application of this method within our SLA framework would be problematic since it would introduce an iterative incremental step in which shear stiffnesses would need to be recomputed for each existing crack plane during each scaled linear analysis. A similar approach to ours was used in a traditional SLA implementation to decrease the shear modulus based on the minimum value of sawtooth Young's modulus between two orthogonal planes [20]. Other models exist for shear retention during tensile cracking [e.g. 52], but few actually have a good physical justification. Ideally, both the Young's and shear moduli (as well as other stiffness parameters) would each depend on both the normal and shear stresses/strains. In other words, a more accurate analysis would include normal-shear coupling. [38] have considered this issue as well, stating that the normal-shear coupling relation is rarely known. Rots and Blaauwendraad [38] argued that relating shear stiffness reduction to degrading properties in the normal direction, as we have done in this work, would at least recover some part of the neglected normalshear coupling interaction.

3.3.2. Updating crack properties during SLA

The process by which potential or existing crack plane properties of element crack plane i are updated during a scaled linear analysis within the SLA procedure is now discussed. From methods described in the Section 3.3.1, the stepwise sawtooth reductions in model I and mode II moduli, as well as in tensile strength, for element crack plane i are defined. For the current sawtooth j of element crack plane i, the mode I and mode II moduli are $D^I_{i:j}$ and $D^{II}_{i:j}$, respectively. Knowing both $D^I_{i:j}$ and $D^{II}_{i:j}$, one can calculate \mathbf{D}^{cr}_i using (25). Finally, the element elastic stiffness matrix \mathbf{D} is updated using (24). The previous element crack plane tensile strength at sawtooth j-1 is $f^+_{i:i:j-1}$; it is updated for sawtooth k in the same way as the conventional SLA method, i.e., the updated tensile strength is simply $f^+_{t:i:j}$.

One notable feature of the current SLA implementation is that, due to the incorporation of the multi-directional crack method, the mode I and

mode II crack moduli $D^I_{i;j}$ and $D^{II}_{i;j}$ are reduced as cracking progresses along an existing element crack plane. In the conventional implementation presented by Slobbe [20], the Young's and shear moduli along a single fixed crack plane were reduced. From another perspective, the current implementation updates the properties relating stresses to crack strains along an existing element crack plane, whereas the conventional implementation updates the properties relating stresses to total strains along a single fixed element crack plane. We note however that the two approaches are closely related since the stepwise reductions in $D^I_{i;j}$ and $D^{II}_{i;j}$ are determined using the sawtooth values $E_{i;j}$.

3.4. Outline of analysis procedure

Prior to performing an FE SLA crack analysis using the proposed methodology, it is necessary to set up a number of analysis parameters. The following sections describe (1) the initial setup in which analysis parameters are assigned to finite elements in the mesh and (2) the procedural steps of a typical numerical analysis using the proposed methodology.

3.4.1. Initial setup of material parameters

Before an FE SLA crack analysis is started, the necessary analysis parameters which govern the constitutive behavior of the finite elements must be defined. In the current analyses, the finite elements are constant strain triangular elements containing a single integration point. Although higher order elements can be used which may yield superior results in certain cases [20], constant strain triangles containing a single integration point are used for the purposes of demonstrating our methodology. Since each element contains a single integration point, parameters assigned to an integration point are assigned to the element as a whole. For each element within the mesh, a set of potential element crack planes are first defined. Potential element crack planes represent the directions within elements along which cracks are allowed to form. For this reason, one can a priori define many potential crack planes in each element to properly capture the yet unknown crack directions. In the current work, each element in the mesh contains 180 potential crack planes over a span of 180 degrees; in other words, relative to the global x-axis, potential crack planes are defined at 0°, 1°, 2° ... 178°, 179°. Due to symmetry, potential crack planes need not be defined past 179°. After defining the crack planes in each element, the crack band width is determined for each plane using methods described in Section 3.1. Next, elastic stiffnesses are assigned to each finite element. In general, elastic stiffnesses may be anisotropic. For analyses of polycrystalline topologies derived from maps of electron backscatter diffraction data, the anisotropic stiffnesses assigned at each integration point may depend on the corresponding crystallographic orientations. In cases such as these, the anisotropic stiffnesses in the crystal coordinate systems should be transformed into the analysis coordinate system prior to performing the analysis [47]. After assigning elastic stiffnesses to each element, it is necessary to assign a material softening law to each potential crack plane within each element. In the current implementation, it is assumed that material behavior in the post-peak regime follows a linear softening law in which the tension softening modulus $E_{t:i}$ for potential crack plane i in is given by

$$E_{t,i} = \left(\frac{1}{E_i} - \frac{2G_{f,i}}{f_{t,i}^2 l_{c,i}}\right)^{-1},\tag{31}$$

where E_i is the Young's modulus in the direction normal to crack plane i determined from the element's elastic stiffness matrix, $G_{f;i}$ is the fracture energy, $f_{t;i}$ is the tensile strength, and $l_{c;i}$ is the crack band width. Note that in general for each crack plane within an element, a different softening law may be defined based on crack plane-specific values of the aforementioned material properties. Once the softening law for each plane i in every element comprising the FE mesh is defined, each softening curve is approximated by generating a sawtooth representation according to the methods described in [20]; subsequently, the crack

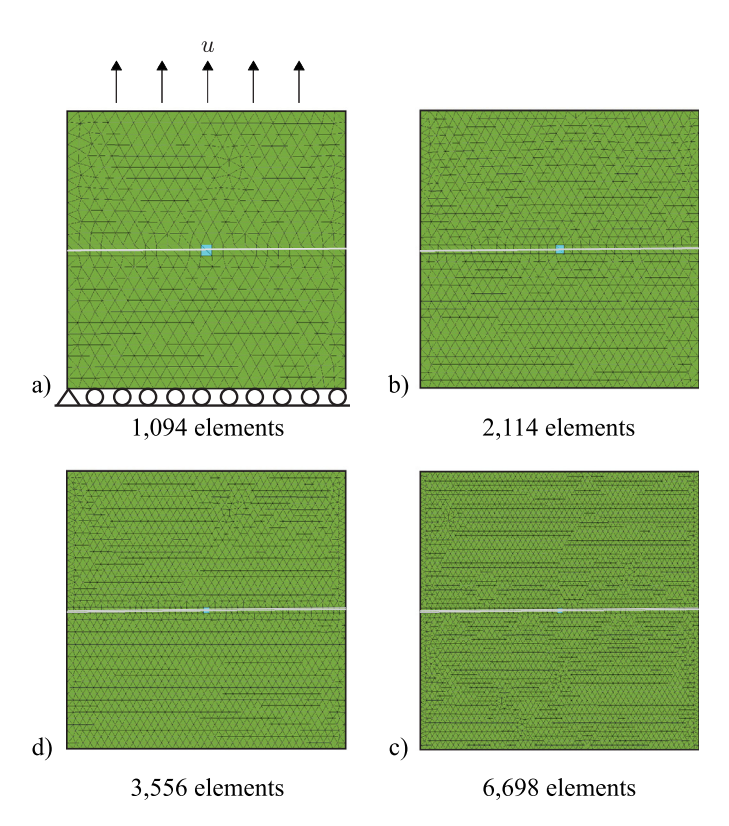


Fig. 6. Square epoxy specimens analyzed in the first validation study. The loading scenario is shown in (a). For each mesh, the resulting crack pattern is shown as a gray line. Also shown in light blue are the pairs of elements at the center of the meshes which, in order to start the analyses, are forced to begin cracking first. (For interpretation of the references to colour in this figure legend, the reader is referred to the web version of this article.)

moduli D_i^I and D_i^{II} for each sawtooth j are computed using the sawtooth Young's moduli $E_{i:j}$ (see Sections 3.3.1 and 3.3.2). Finally, crack moduli $D_{i:j}^I$ and $D_{i:j}^{II}$ of sawtooth j, as well as sawtooth tensile strength $f_{t:i:j}^+$, are stored for each potential element crack plane i in the FE mesh.

3.4.2. FE SLA procedure

Once the material properties are defined using the details of Section 3.4.1, the FE SLA crack analysis is initiated. The analysis boundary conditions are first defined (i.e., applied reference displacements or tractions and fixed node information) by adjusting the appropriate entries in the initial global stiffness matrix and the initial global force vector [53]. The FE SLA analysis begins by computing the nodal displacements due to the applied reference loads. Next, the nodal displacements are used to compute the element strains and stresses. The element stresses are then used to determine the normal stresses on each existing or potential element crack plane. Subsequently, the element crack plane normal stresses are used in conjunction with the current sawtooth tensile strengths to determine the ratio r_i of normal stress to current tensile strength for each existing and potential element crack plane i in each element of the FE mesh. At this juncture, the crack tracking algorithm history is consulted to determine the elements whose existing and potential crack planes are allowed to be selected as the critical element crack plane. Generally, the ratios r_i of each potential crack plane that are in an element that is neither an isolated element, nor an intersected element, nor a cracked element, are set to zero. The critical element crack plane icrit is then taken as the element crack plane having the greatest normal stress to current tensile strength ratio, defined as r_{crit} , and the critical load factor λ_{crit} is computed as the $1/r_{crit}$. After determining the critical element crack plane, the displacements, stresses and strains are scaled by λ_{crit} . According to the details in Section 3.3.2, the current crack mod-

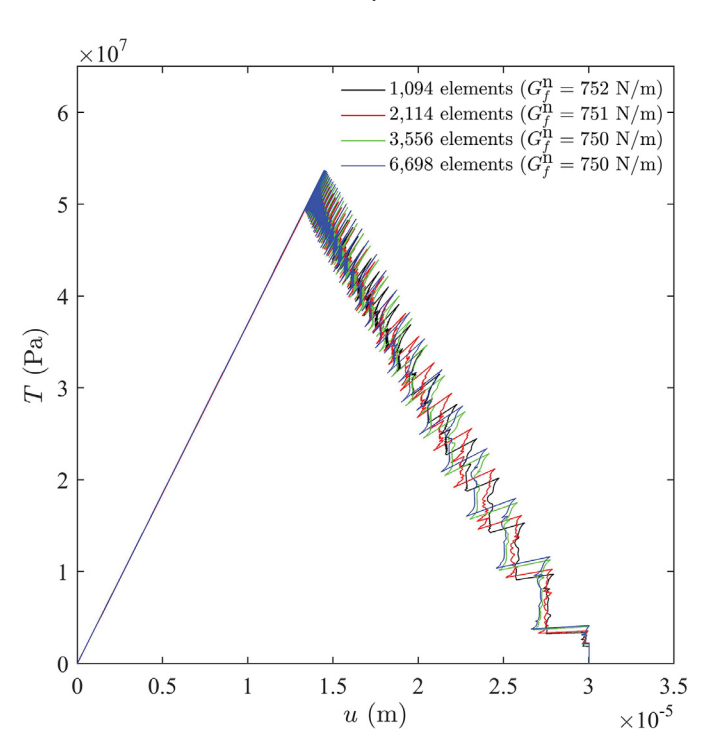


Fig. 7. Resulting traction vs. displacement curves for the meshes shown in Fig. 6. For each mesh density listed in the legend, the corresponding numerically calculate fracture energy is given.

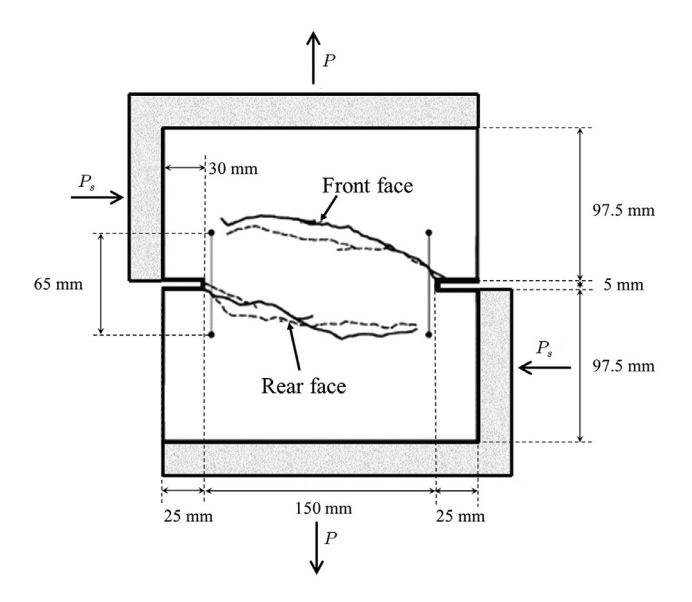


Fig. 8. Experimental setup and failure cracks for the DEN specimen Nooru-Mohamed [54].

uli $D^I_{i_{crit};j}$ and $D^{II}_{i_{crit};j+1}$ corresponding to the critical crack plane i_{crit} are reduced to $D^I_{i_{crit};j+1}$ and $D^{II}_{i_{crit};j+1}$, and the elastic stiffness matrix $\mathbf{D}_{e_{crit}}$ corresponding to critical element e_{crit} is updated. Subsequently, the global stiffness matrix and global force vector entries corresponding to e_{crit} are updated to reflect the new values in $\mathbf{D}_{e_{crit}}$. At this point, the user-defined termination criterion is checked. If the termination criterion has not yet been achieved, the process restarts by computing new nodal displacements using the updated global stiffness matrix and global force vector. This loop is continued until the termination criterion is achieved, or the user manually stops the FE SLA analysis.

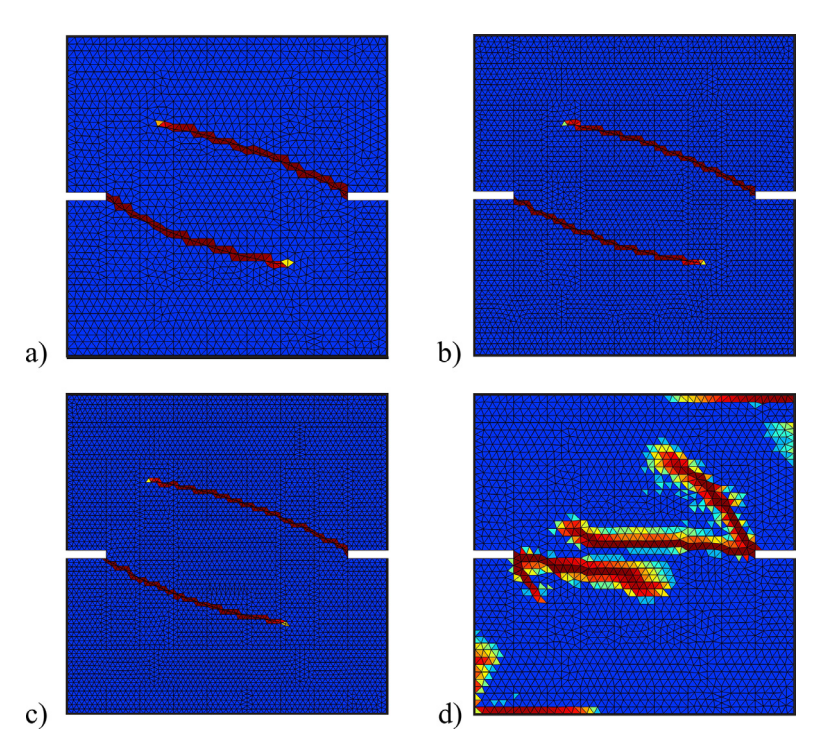


Fig. 9. Crack path results for DEN specimen. Meshes in shown in (a) though c) contain 3,640, 6,936, and 9006 elements, respectively. Crack propagation in plots (a)—(c) are controlled by the crack tracking algorithm. Cracking in the mesh shown in (d), having 3640 elements, is not guided by a crack tracking algorithm; instead, any element plane is allowed to crack if it is selected as the critical plane during an SLA run.

4. Validation of objectivity of results

In this section, two validation studies are performed to demonstrate objectivity of results with respect to characteristics of the FE mesh. In the first study, objectivity is demonstrated with respect to element size sensitivity. The current implementation of the smeared crack band approach leads to results for dissipated energy during cracking that do not depend on the element size. In the second study, the well-known double-edge notched specimen is considered to demonstrate objectivity with respect to directional mesh bias. In this case, objectivity is achieved through the use of the crack tracking algorithm described in Section 3.2. In both studies, there are 180 potential crack planes defined a priori within each finite element and each potential element crack plane material softening law is approximated by a step-wise sawtooth curve with 30 sawteeth.

4.1. Validation study #1: element size sensitivity

As first described by Bazant and Oh in [6], the smeared crack band concept provides objective results in an FE analysis regardless of the size of finite elements. In other words, the energy dissipated during cracking does not depend on the size of finite elements. To illustrate objectivity with respect to element size, a similar study to that presented by Pineda et al. [39] is performed. As shown in Fig. 6a, a uniform, uniaxial, vertical displacement u is applied to a monolithic square specimen. The specimen is composed of MY750/HY917/DY063 epoxy with Young's modulus $E_0 = 3.7$ GPa, Poisson's ratio v = 0.35, critical strain at peak stress $\varepsilon_c = 0.0135$, and mode I fracture energy $G_f = 750 \text{ J/m}^2$ [39]. It is assumed that the epoxy softens linearly in the post-peak regime. As mentioned in [39], the material properties are chosen to show significant energy dissipation during cracking. The four different meshes shown in Fig. 6(a-d) containing 1,094 elements, 2114 elements, 3556 elements, and 6698 elements, respectively, are considered. The resulting vertical traction T vs. the applied vertical displacement u is shown in Fig. 7. In the current analyses, cracking is forced to begin in the two center-most elements of the mesh (light blue elements in Fig. 6) by defining these

elements as isolated elements a priori, after which cracking is governed by the crack tracking algorithm. As shown in Fig. 7, the resulting T vs. u curves demonstrate objectivity with respect to element size in terms of peak load, softening behavior, and dissipated energy. For these analyses, the dissipated energy due to fracture is G_f , i.e., the area under the T vs. u curve. The values of G_f^n , where the superscript n denotes the numerically obtained value, are shown in the legend of Fig. 7, each of which are close to the prescribed value of 750 N/m. The scattered nature of the T vs. u curves is characteristic of the SLA method due to the discontinuous nature in which the properties of crack planes are updated; a (u, T) data point is added to the T vs. u curve each time a crack plane i within an element is selected as the critical crack plane and has its crack moduli D_i^I and D_i^{II} decreased from sawtooth j to sawtooth j+1. (see Section 3.3.2). It is also noted that the frequencies of the curves in Fig. 7 are shown to be dependent on the number of sawteeth used to approximate the softening relations, futher demonstrating the mesh objectivity of the methodology. The resulting crack paths for each analysis are superimposed on the FE meshes shown in Fig. 6(a-d) as gray lines. In these analyses, the crack tracking algorithm has ensured that the resulting crack propagate along a horizontal line at the vertical center of the mesh. Given the uniaxial loading scenario and the structured mesh, the resulting crack paths in the absence of a crack tracking algorithm are expected follow similar propagation paths to those shown in Fig. 6 (a-d). In the next validation study, a more complex loading case is considered in which directional mesh bias significantly affects crack path results in the absence of a crack tracking algorithm.

4.2. Validation study #2: Mesh directional bias

In this next validation study, the effectiveness of the crack tracking algorithm (see Section 3.2) is tested. The well-known double-edge notched (DEN) specimen test of Nooru-Mohamed [54] is considered. The experimental setup, including specimen dimensions and applied loads, as well as the resulting crack paths, are shown in Fig. 8. In the original experiment, specimens of 50 mm thickness were subjected first to an increasing lateral shear displacement until the resulting load

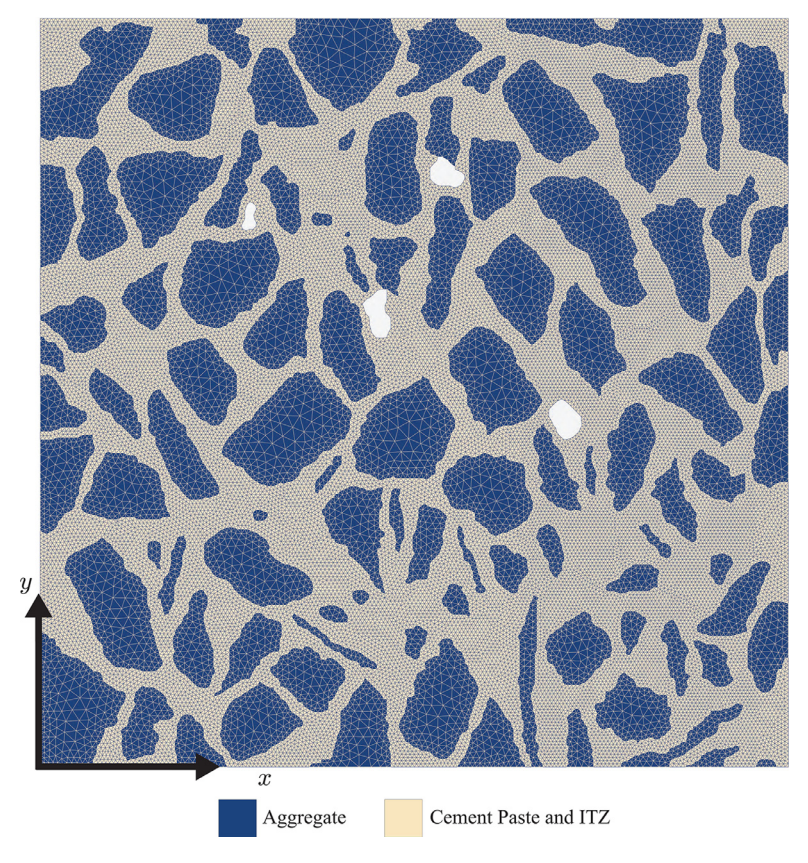


Fig. 10. Concrete morphology and finite element mesh. Since cracking is only allowed in the cement paste and ITZs (tan phase), the analysis runtime is reduced by increasing the size of the elements within the aggregates.

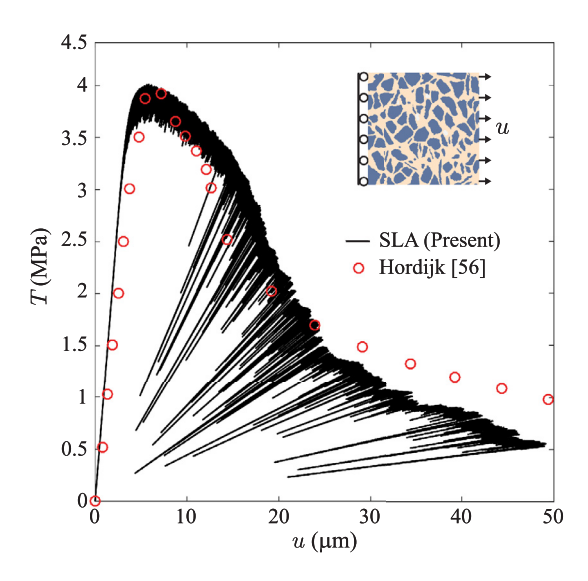


Fig. 11. Resulting SLA traction-displacement curve for horizontal uniaxial loading of the concrete microstructure in Fig. 10 compared with experimental results of Hordijk [56].

 $P_S=10$ kN, while the vertical load was kept at P=0 kN. Subsequently, the shear load was held constant at $P_S=10$ kN and an increasing displacement in the vertical direction was applied to the top and bottom edges of the specimen. Several other authors have also numerically simulated this test [12,20]. In this analyses, the simplification introduced by Slobbe [20] is used in which the vertical load P is applied at the same time as the shear load P_S . Slobbe [20] justified this simplification since the free vertical deformation of the specimen during experimental tests was negligible. It is likely the case as well that the assumption was made

due to the fact that the standard SLA method cannot properly handle non-proportional loading. DeJong et al. [12] have extended the SLA method for certain types of non-proportional loading, but additional effort must be made to generalize SLA for all cases. The specimen considered is composed of plain concrete with Young's modulus $E_0 = 30$ GPa, Poisson's ratio v = 0.2, tensile strength $f_t = 3$ MPa, and mode I fracture energy $G_f = 100 \text{ J/m}^2$ [20]. Although more accurate softening models exist for concrete [e.g. 55], for the purpose of validating the resulting numerically-generated crack paths with those of Nooru-Mohamed [54], a linear softening relationship is assumed for the element crack planes [6]. The meshes studied here contain horizontal rows of elements and have been tailored this way to explicitly introduce some directional mesh bias. As shown, the computed cracks for the different meshes in Fig. 9(a-c) show similar patterns and are qualitatively similar the experimental results of [54] displayed in Fig. 8. Fig. 9d shows the resulting cracking behavior in the absence of the crack tracking algorithm for the same mesh as in Fig. 9a. In the analysis of Fig. 9d, the crack tracking algorithm was nullified by a priori classifying each element in the FE mesh as an isolated element; results for this analysis reveal strong sensitivity to the mesh geometry. Similar results were found by Slobbe [20] who, in considering various element types, found that superior crack paths emerged for various element types in analyses which employed a crack tracking algorithm. Crack paths numerically generated by DeJong et al. [12] without a crack tracking algorithm did not compare as well with [54], even though non-proportional loading was simulated. However, DeJong et al. [12] found that randomly generated meshes lacking clearly defined mesh lines improved results to some extent.

5. Results and discussion

In the following section, the proposed methodology is illustrated by considering two model problems. In the first model problem, a concrete

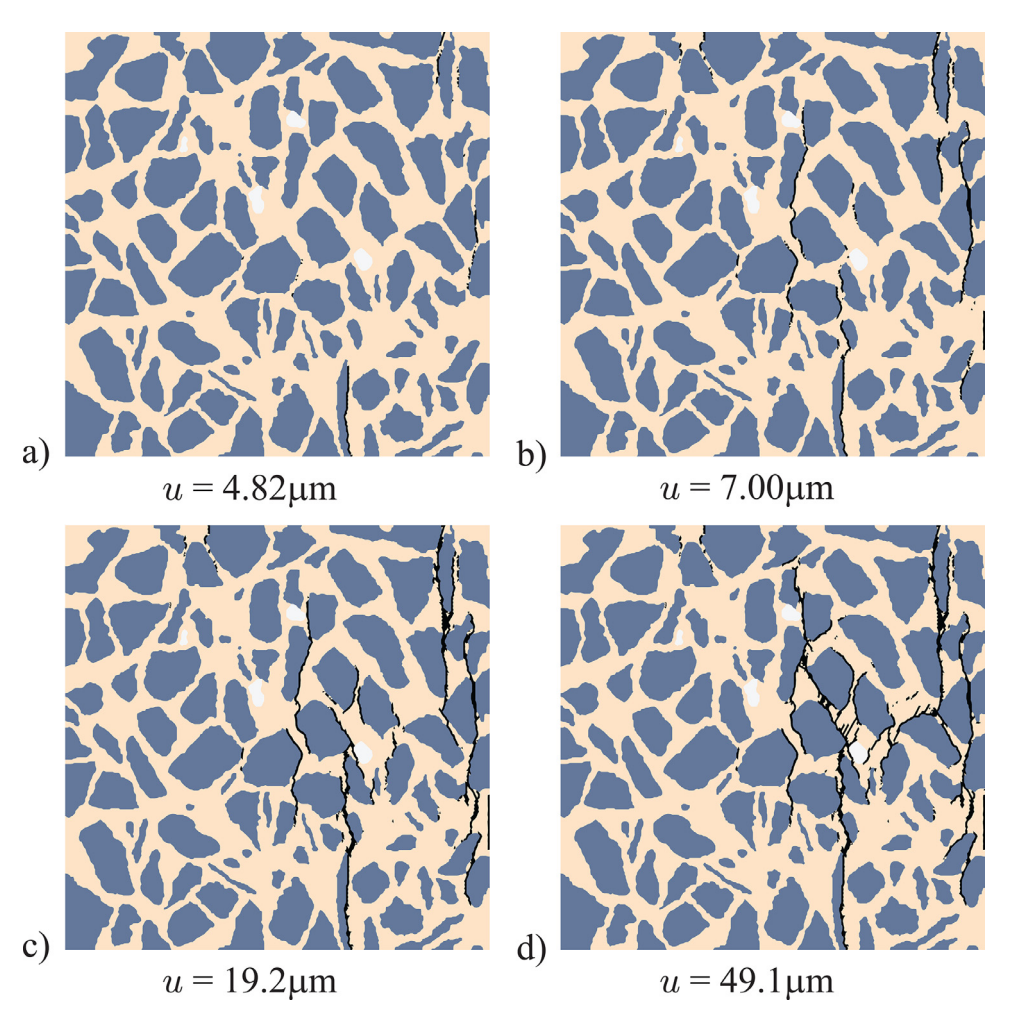


Fig. 12. Cracked element patterns in concrete sample at four different stages during a horizontal uniaxial loading analysis. Elements shown in black have reduced Young's moduli that are less than 10% of their initial values. Provided below each subfigure are the corresponding applied displacements.

morphology from Ren et al. [33] subjected to a uniaxial tensile load is considered. Results for the bulk traction-displacement behavior, as well as the developed crack patterns, are compared with results from the literature. In the second model problem, we consider a computer-generated polycrystalline alumina microstructure and present results for bulk traction-displacement behavior and crack patterns resulting from uniaxial and simple shear loading cases. In addition, the influence of grain boundary strength on the resulting crack patterns is studied.

5.1. Model problem 1 - Heterogeneous concrete

In this section, a concrete morphology generated using X-ray computed tomography is studied using our proposed methodology. The 37.2 mm concrete cross-section considered here (see Fig. 10) has been taken from [33]. In order to generate a mesh for the concrete morphology, we have copied the image from [33], removed anti-aliasing, and enlarged it to its original size of 372x372 pixels. After modification, the phase volume fractions of the aggregates, the cement paste, and the voids were found to be 0.519, 0.476, and 0.005, respectively (compared to the original volume fractions of 0.518, 0.477, and 0.005 listed in [33]). The aggregate and cement paste phases are shown in blue and tan, respectively, in Fig. 10. Using the meshing technique outlined in Section 3, the concrete morphology is discretized with 60,000 constant strain triangular elements with a single integration point each. The concrete phase distribution and the generated FE mesh are shown in Fig. 10. Within each element, 180 potential crack planes are defined. Each plane is assumed to deform by linear softening in the post peak

 Table 1

 Phase properties for concrete cross-section Ren et al. [32].

Phase	E (GPa)	ν	f_t (MPa)	G_f (N/m)
Aggregate	70	0.20	-	-
Cement paste	25	0.20	6.0	60
ITZ	25	0.20	3.0	30

regime. The linear softening curve for each plane is approximated using a representative sawtooth curve with 30 sawteeth (see Section 3.4.1). Interface transition zones (ITZs) are introduced within the cement paste phase to more accurately model actual concrete. In our implementation, the ITZs are modeled within the cement paste phase as the band of elements which lie on the outside boundary of aggregate inclusions. A similar approach has been made by Huang et al. [34] in their analysis of concrete microstructures obtained from X-ray computed tomography. The Young's modulus E, Poisson's ratio v, tensile strength f_t , and fracture energy G_f for the different phases are listed in Table 1. Note that in Table 1, the dash symbol signifies that the corresponding property is not needed in the analysis. For example, cracks are prohibited from traveling through elements of the aggregates, and therefore aggregate fracture properties do not need to be specified. Cracks can only propagate through the elements of the cement paste and the ITZs. Note that the ITZ elements are assigned the same elastic properties as the cement paste but are given reduced fracture properties f_t and G_f which are equal to 60% of the corresponding cement paste properties. Note also that the

voids are discretized using finite elements but are assigned a stiffness eight orders of magnitude less than the cement paste (see Table 1). As is evident from the properties listed in Table 1, each phase in this model problem is treated as isotropic, and therefore all planes within an element have the same initial elastic and fracture properties. For this study, all ITZ elements are a priori classified as isolated elements and therefore all existing and potential crack planes in these elements are considered when determining the critical element crack plane during any scaled linear analysis of the SLA procedure. Crack planes in the elements comprising the cement paste are considered only if they have been selected by the governing crack tracking algorithm.

A uniaxial tension test is simulated by horizontally fixing the nodes on the left boundary of the mesh (x=0), and by subjecting the nodes on the right boundary of the mesh to a uniformly distributed horizontal displacement u (positive x-direction) (see Fig. 11 inset). Fig. 11 shows the resulting SLA traction T vs. displacement u curve for the concrete morphology considered here, as well as the experimental results from Fig. 40 of [56]. The curve determined using the proposed methodology compares well with the experimental results of [56] for the selected reduced fracture properties of the ITZ elements. However, the concrete morphology considered here is not the same as the one considered in [56]; as a result, one should only compare the two sets of results in a qualitative manner. The peak strength determined from Fig. 11 is found to be 4.01 MPa, which is close to the peak strength of roughly 3.9 MPa from [56]. Furthermore, the gradual decrease in T with increasing u is qualitatively similar to the softening behavior shown in [56].

In addition to the traction-displacement curves, we also compare the resulting crack patterns with those presented by Ren et al. [33] for the same concrete morphology subjected to the same loading conditions. Fig. 12 shows the crack patterns resulting from the proposed methodology at four different stages during the analysis. Only elements containing an existing crack plane whose Young's modulus has decreased below 10% of its original value are shown in Fig. 12 (black elements). The applied displacement u corresponding to the state of cracking in the microstructure is provided below each crack plot and corresponds to the values along the horizontal axis in Fig. 11. In comparison to the results provided in [33], our methodology produces similar non-dominant crack patterns in roughly the same areas. As shown, more cracks tend to form on the right side of the microstructure within ITZ elements, and ultimately two dominant cracking regions emerge (displayed in black in Fig. 12d). One dominant region extends up from the bottom of the microstructure, and is horizontally located just to the right of the horizontal center. The second dominant crack region begins near the upper right corner of the microstructure and extends down the right side. The two dominant cracks which emerge in our analysis appear to coincide with the dominant cracks presented in [33]. This, along with the comparisons made between our bulk traction-displacement curves and the experimental results of [56], demonstrate the applicability of the proposed methodology to such analyses.

5.2. Model problem 2 - Polycrystalline alumina

In this model problem, a computer-generated Voronoi-like microstructure containing 122 grains is considered (see Fig. 13). The microstructure is assumed to be composed of anisotropic alumina grains with random crystallographic orientations. The single-crystal elastic properties of alumina are taken from [57] and listed here in matrix form

$$\mathbf{D}_{Al_20_3} = \begin{bmatrix} 500.1 & 161.7 & 111.4 & -23.26 & 0 & 0\\ 161.7 & 500.1 & 111.4 & 23.26 & 0 & 0\\ 111.4 & 111.4 & 502.4 & 0 & 0 & 0\\ -23.26 & 23.26 & 0 & 151.0 & 0 & 0\\ 0 & 0 & 0 & 0 & 151.0 & -23.26\\ 0 & 0 & 0 & 0 & -23.26 & 169.2 \end{bmatrix} \mathbf{GPa}$$
(32)

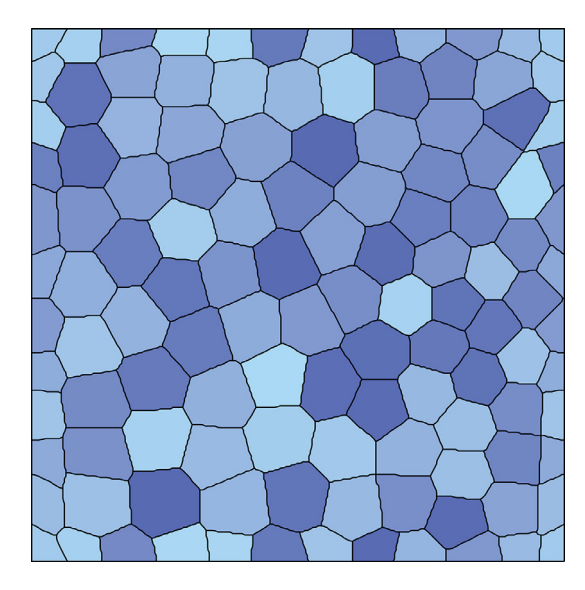


Fig. 13. Voronoi-like computer-generated microstructure for alumina studies. The different shades of blue represent the different (random) crystallographic orientations. (For interpretation of the references to color in this figure legend, the reader is referred to the web version of this article.)

The following analyses use single-crystal alumina fracture properties in which the average grain tensile strength f_t is 400 MPa, and the fracture toughness K_{IC} is 1.5 MPa m^{1/2} [58]. The value of fracture energy for a plane is determined using the plane stress relation $G_f = K_{IC}^2/E$. Since the Young's modulus generally varies from plane to plane for an anisotropic material, the fracture energy G_f also varies. In order to perform FE analyses, the microstructure in Fig. 13 is discretized by an FE mesh containing 60,074 elements. Each element contains 180 potential crack planes. Each potential crack plane obeys a linear softening law once its tensile strength has been exceeded. The linear softening curves for each element plane are discretized by 30 sawteeth for use within the SLA method. In regards to crack initiation, elements with a node at triple-junction points, i.e., points where the boundaries of three or more grains intersect, are locations of concentrated stresses and therefore generally experience higher stresses than other elements in the mesh (with the possible exceptions of cracked and intersected elements). Therefore, elements with a node at triple-junction points are defined a priori as isolated elements; intergranular and transgranular propagation of cracks into surrounding elements is then governed by the crack tracking algorithm (see Section 3.2). It is assumed that the average grain size of alumina is 2 µm, which is within the range reported by Seidel et al. [59]. In our experience, this choice of grain size appears to produce a slightly less brittle response in the traction-displacement curves as compared to larger grain sizes. Parametric studies which consider the influence of grain size [e.g. 60] can be performed using the current methodology, although such studies are not considered here.

5.3. Dependence of crack path on grain boundary strengths for a uniaxial load

In this study, the influence of grain boundary strength on the development of intergranular and transgranular cracking is considered. Zavattieri and Espinosa [60] have studied intergranular cracking in brittle materials using a two-dimensional stochastic finite element analysis which incorporated cohesive elements along grain boundaries. Here, a vertical uniaxial displacement load shown in the inset of Fig. 15a is applied in three different analyses in which the grain boundary strength is reduced compared to the grain interior strength. In the first, second, and third analyses the grain boundary strengths $f_t^{\,gb}$ are $0.5\,f_t^{\,int}$, $0.7\,f_t^{\,int}$, and $0.9\,f_t^{\,int}$, respectively, where $f_t^{\,int}$ is the tensile strength of the grain interior. It is noted that for this study the fracture toughness K_{IC} assigned

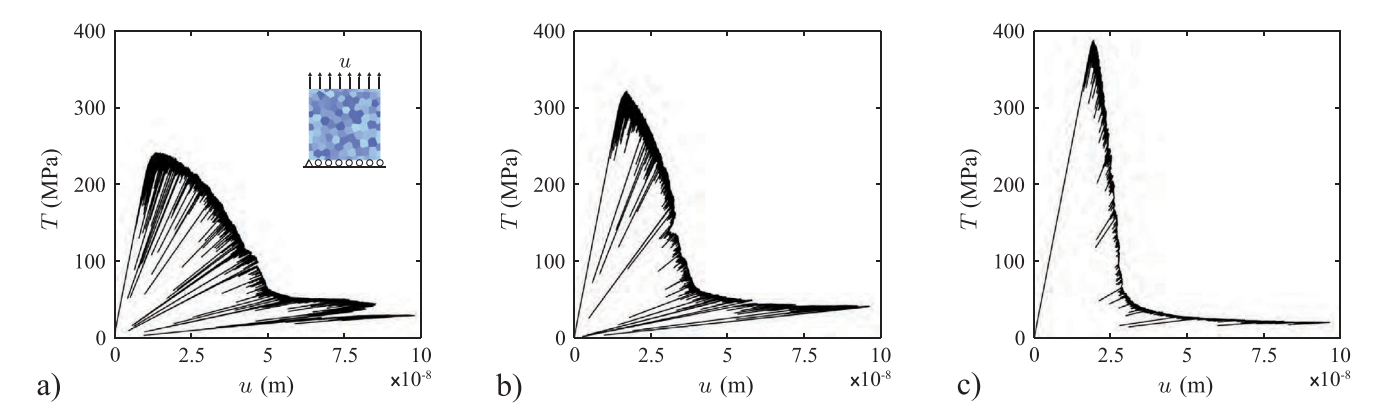


Fig. 14. Resulting traction-displacement curves for three uniaxial loading analyses of an alumina microstructure with different grain boundary strengths f_i^{gb} which are less than the grain interior strength f_i^{pit} . a) $f_i^{gb} = 0.5 f_i^{int}$, b) $f_i^{gb} = 0.7 f_i^{int}$, c) $f_i^{gb} = 0.9 f_i^{int}$.

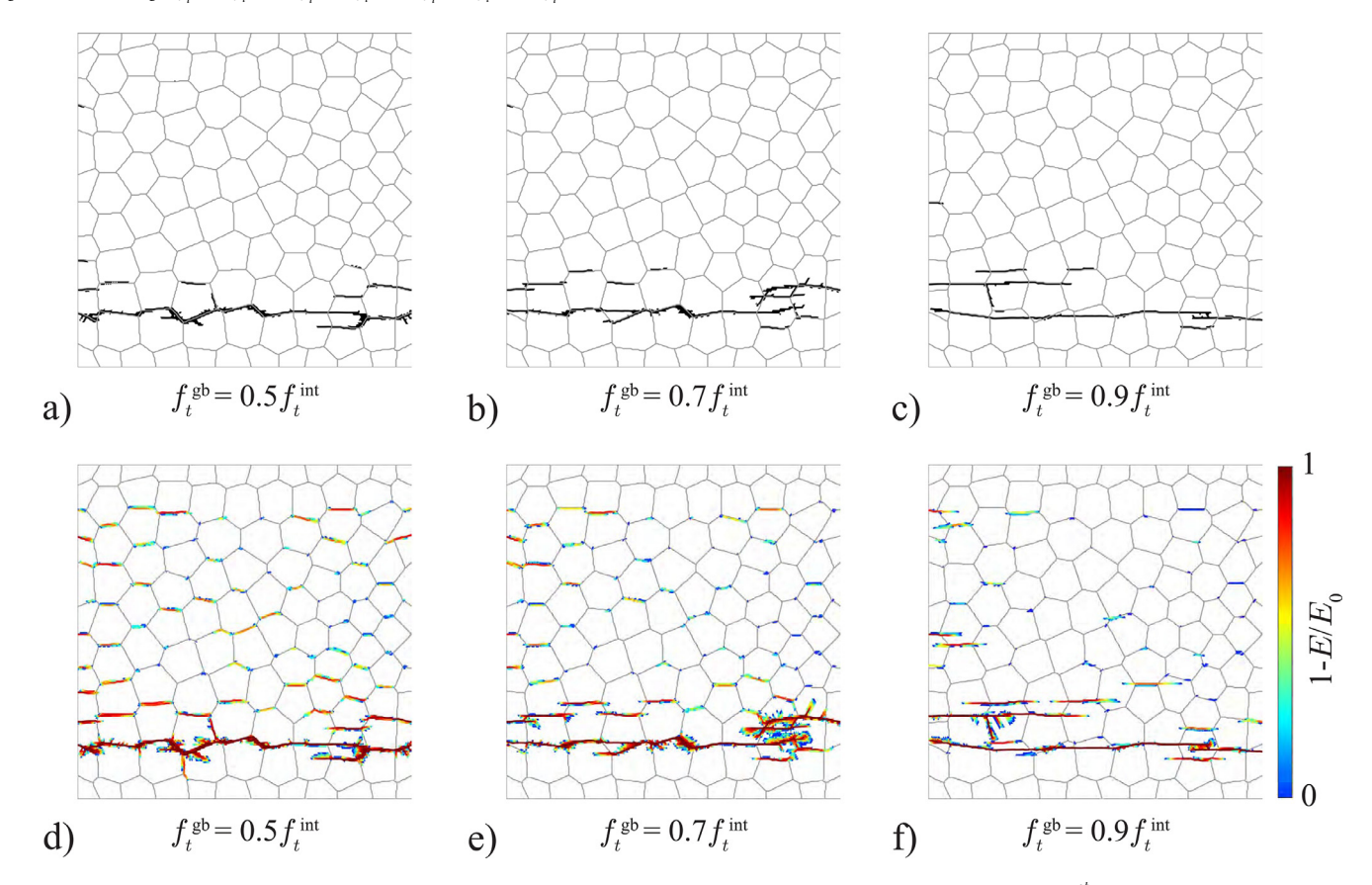


Fig. 15. Resulting crack patterns for three uniaxial loading analyses of an alumina microstructure with different grain boundary strengths f_i^{tb} which are less than the grain interior strength f_i^{im} . (a-c) Elements containing crack planes with Young's moduli that have decreased to less than 10% of the initial values, and (d–f) all elements containing crack planes. Element colors are defined by the color bar and are based on the expression $1 - E/E_0$, where E and E_0 are a crack plane's current and initial Young's moduli, respectively. For elements containing multiple crack planes, the plane with the greatest value defined by $1 - E/E_0$ is used. (For interpretation of the references to color in this figure legend, the reader is referred to the web version of this article.)

to the grain boundaries is not reduced relative to that assigned to the grain interiors.

Fig. 14 and Fig. 15 show the results for the three alumina analyses performed with reduced grain boundary tensile strengths. In Fig. 14(a-c), the traction-displacement curves are shown for the grain boundary strengths $0.5f_t^{\rm int}$, $0.7f_t^{\rm int}$, and $0.9f_t^{\rm int}$. As can be seen, the peak strength increases with increasing grain boundary strength. The peak strengths for the cases shown in Fig. 14(a-c) are approximately 241 MPa, 322 MPa, and 388 MPa, respectively. The three plots in Fig. 14(a-c) show that the overall slope of the traction-displacement curve increases with increasing grain boundary strength, i.e., the response becomes more brittle. This behavior is expected since the fracture energy assigned to every element crack plane in all three analyses is the same.

Fig. 15(a–c) shows the cracked elements which contain crack planes with Young's moduli in the normal direction that have decreased to less than 10% of their initial values. In other words, if E and E_0 are a crack plane's current and initial Young's moduli, then the element containing the crack plane is shown if $1-E/E_0 \geq 0.9$. The crack patterns correspond to the maximum displacements on the traction-displacement curves shown in Fig. 14 (note that all maximum displacements have similar values). Fig. 15(a–c) correspond to the reduced grain boundary strengths of $0.5f_t^{\rm int}$, $0.7f_t^{\rm int}$, and $0.9f_t^{\rm int}$, respectively. As can be seen, almost all cracks in the case of $f_t^{\rm gb}=0.5f_t^{\rm int}$ are within elements which lie along grain boundaries. For $f_t^{\rm gb}=0.7f_t^{\rm int}$, a couple cracks have propagated either through or into grain interiors. For $f_t^{\rm gb}=0.9f_t^{\rm int}$, cracks

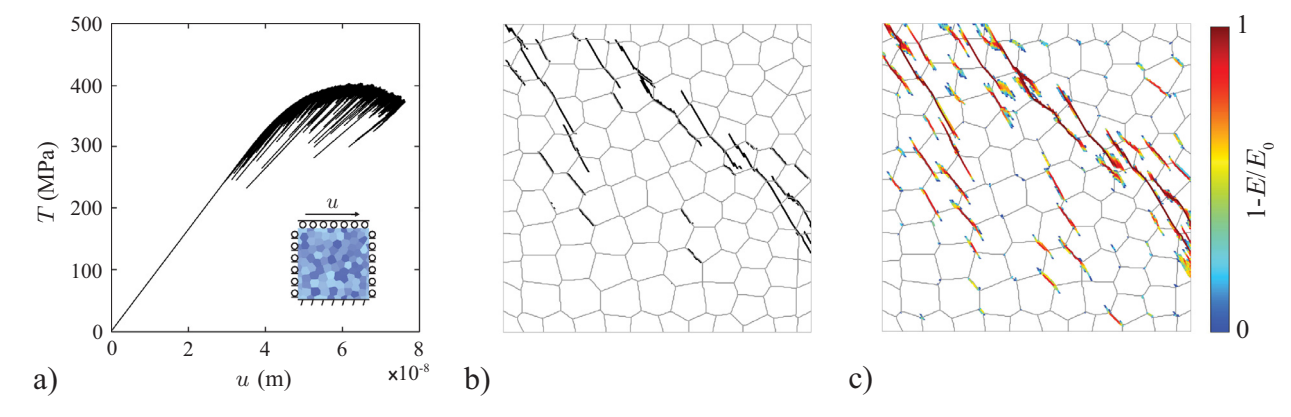


Fig. 16. Results for a simple shear loading analysis of an alumina microstructure with grain boundary strengths $f_i^{gb} = 0.7 f_i^{int}$ where f_i^{int} is the grain interior strength. (a) Traction T vs. applied displacement u curve, where T is taken as the sum of nodal forces along the top surface in the direction of applied u (see inset for load and boundary conditions), (b) elements containing crack planes with Young's moduli that have decreased to less than 10% of the initial values, and (c) all elements containing crack planes. Element colors are defined by the color bar and are based on the expression $1 - E/E_0$, where E and E_0 are a crack plane's current and initial Young's moduli, respectively. For elements containing multiple crack planes, the plane with the greatest value defined by $1 - E/E_0$ is used. (For interpretation of the references to color in this figure legend, the reader is referred to the web version of this article.)

travel through grains almost as often as they do along the grain boundaries. All dominant crack paths shown in Fig. 15(a–c) appear to travel along the same path near the bottom of the alumina microstructure. Fig. 15(d–f) correspond to the same snapshot in the analysis as Fig. 15(a–c) but show all elements which contain a crack plane. For these analyses, lower grain boundary strengths are accompanied by more cracks throughout the microstructure; The number of non-dominant cracks is greatest for $f_t^{\rm gb}=0.5f_t^{\rm int}$ and least for $f_t^{\rm gb}=0.9f_t^{\rm int}$. These results correspond with the softening behavior shown in Fig. 14; for example, given the pervasiveness of non-dominant cracks in Fig. 15-d compared to Fig. 15f, one would expect a less brittle response in Fig. 14a than in Fig. 14c. In all three cases, the microstructure ultimately fails along a single dominant crack which is approximately normal to the vertical loading direction.

5.4. Results for simple shear loading

In this final study, we simulate the early stages of cracking in the alumina microstructure due to simple shear loading. The main objective of this analysis is to show that the proposed methodology produces cracks which have appropriate orientations relative to the applied load and boundary conditions (see Fig. 16a inset). We assume that the grain boundary strengths $f_t^{\rm gb} = 0.7 f_t^{\rm int}$, where $f_t^{\rm int}$ is the tensile strength of the grain interior. Other analysis parameters used here are the same as those used in the analyses of Section 5.3.

Fig. 16 shows the results for the simple shear analysis of the alumina microstructure. Fig. 16a shows the traction T versus applied displacement *u* relationship for early stages of cracking (see Fig. 16a inset), where *T* is computed as the sum of the nodal forces along the top surface of the microstructure in the direction of applied u. The peak value of T is roughly equal to the assumed tensile strength of alumina i.e., 400 MPa. As shown in Fig. 16a, the peak of the T - u curve is followed by softening behavior. Fig. 16b show the cracked elements which contain crack planes with Young's moduli in the normal direction that have decreased to less than 10% of their initial values. The crack patterns correspond to the maximum displacements on the T-u curve shown in Fig. 16a. As expected, the dominant cracks of Fig. 16b lie at an angle of roughly 135 degrees to the x-axis and tend to travel along grain boundaries more often than grain interiors due to the reduced grain boundary strength. Fig. 16c corresponds to the same snapshot in the analysis as Fig. 16b but shows all elements which contain a crack plane. It is noted that cracking is more prevalent along grain boundaries which are roughly parallel to the dominant crack directions.

6. Conclusions

A numerical methodology has been presented for the analysis of pervasive cracking in heterogeneous materials. The smeared crack band concept is used in conjunction with the multi-directional crack model to objectively model cracking in a finite element analysis while allowing cracks to form at different orientations. In order to reduce the stress locking prevalent in existing fixed crack models, multiple cracks are able to form within a finite element. An advanced meshing technique is used in order to generate mesh with smooth grain boundaries and highquality elements of uniform size. The sequentially linear analysis procedure is used in place of an iterative method to avoid instability issues and to capture the snap-type behavior of brittle materials. The implementation is generalized to allow for the analyses of heterogeneous materials composed of anisotropic constituents; furthermore, elastic stiffnesses and fracture parameters of the materials studied can vary with orientation. A crack tracking algorithm is formulated to mitigate the effects of directional mesh bias. Although plane stress conditions are used presently, appropriate generalizations to the formulations herein could allow for the study of plane strain and full three-dimensional problems. Validation studies are performed to ensure the objectivity of results with respect the geometry of the finite element mesh. In order to illustrate the proposed methodology, two models problems are performed. In the first, cracking in a concrete microstructure obtained using X-ray computed tomography is studied. Bulk constitutive behavior and crack patterns are compared with results of other crack methods in the literature. It is found that traction-displacement behavior determined using the proposed methodology compares reasonably well with the corresponding results from a discrete crack finite element analysis using cohesive zone elements. In addition, the dominant cracks generated during the analyses of both methods emerge in the same regions of the concrete microstructure. Next, the proposed methodology is used to analyze cracking within a computer-generated polycrystalline microstructure. The microstructure is composed of Voronoi-like grains which are each assigned the properties of anisotropic alumina. We introduce heterogeneity into the microstructure by assigning each grain a random crystallographic orientation. In order to demonstrate a capability of the proposed methodology, analyses are performed in which grain boundary tensile strengths are reduced compared to grain interiors. It is found that the amount of cracking along grain boundaries increases as the grain boundary tensile strengths are decreased relative to the grain interiors. Stronger grain boundaries are found to produce a more brittle tractiondisplacement softening response. This is supported by the greater number of non-dominant cracks which develop in the case of weaker grain boundaries. In all the three cases considered, the microstructure ultimately fails along a dominant crack which is approximately normal to the applied loading direction. A final study is performed to simulate the cracking in the alumina microstructure due to simple shear loading. The early stage of cracking is accompanied by softening behavior, and dominant cracks tend to travel along grain boundaries due to the reduced tensile strength. It is shown that simple shear produces cracks which propagate at angles of roughly 135 degrees to the *x*-axis. In addition, cracks tend to form along grain boundaries that are roughly parallel to the dominant crack directions.

Acknowledgements

This work was supported by the U.S. National Science Foundation through grants NSF EAR-1015349, EAR-1118786, EAR-1347087, EAR-0820946 and EAR-1150438. In addition, the support provided by the University of Maine to A.C. Cook through a Michael J. Eckardt Dissertation Fellowship is gratefully acknowledged.

References

- Dugdale DS. Yielding of steel sheets containing slits. J Mech Phys Solids 1960;8(2):100–4.
- [2] Barenblatt G. The mathematical theory of equilibrium cracks in brittle fracture. In: Advances in Applied Mechanics, 7. Elsevier; 1962. p. 55–129.
- [3] Ngo D, Scordelis A. Finite element analysis of reinforced concrete beams, 64; 1967. p. 152–63.
- [4] Hillerborg A, Modeer M, Petersson P. Analysis of crack formation and crack growth in concrete by means of fracture mechanics and finite elements. Cement Concrete Res 1976;6(6):773–81.
- [5] Rashid YR. Ultimate strength analysis of prestressed concrete pressure vessels. Nuclear Eng Des 1968;7(4):334–44.
- [6] Bazant ZP, Oh BH. Crack band theory for fracture of concrete. Mater Struct 1983;16(3):155–77. doi:10.1007/BF02486267.
- [7] De Borst R, Nauta P. Non-orthogonal cracks in a smeared finite element model. Eng Comput 1985;2(1):35–46. https://doi.org/10.1108/eb023599.
- [8] ACI. ACI Committee 446 Finite element analysis of fracture in concrete structures: state-of-the-art, USA: American Concrete Institute; 1997. ACI 446.3R-97.
- [9] Cervenka V, Pukl R, Ozbolt J, Eligehausen R. Mesh sensitivity effects in smeared finite element analysis of concrete fracture. Fract Mech Concr Struct, FRAMCOS 1995;2:1387–96.
- [10] Cervera M, Chiumenti M. Smeared crack approach: back to the original track. Int J Numer Anal Methods Geomech 2006;30(12):1173–99.
- [11] De Borst R. Fracture in quasi-brittle materials: a review of continuum damage-based approaches. Eng Fract Mech 2002;69(2):95–112.
- [12] DeJong MJ, Hendriks MAN, Rots JG. Sequentially linear analysis of fracture under non-proportional loading. Eng Fract Mech 2008;75(18):5042–56.
- [13] Gajer G, Dux PF. Crack band based model for FEM analysis of concrete structures. J Struct Eng 1990;116(6):1696–714.
- [14] Gambarova PG, Valente G. Smeared crack analysis for fracture and aggregate interlock in concrete. Eng Fract Mech 1990;35(4):651–63.
- [15] Cervera M, Chiumenti M. Mesh objective tensile cracking via a local continuum damage model and a crack tracking technique. Comput Methods Appl Mech Eng 2006;196(1):304–20.
- [16] Cervera M, Pelà L, Clemente R, Roca P. A crack-tracking technique for localized damage in quasi-brittle materials. Eng Fract Mech 2010;77(13):2431–50.
- [17] Slobbe AT, Hendriks MAN, Rots JG. Smoothing the propagation of smeared cracks. Eng Fract Mech 2014;132:147–68.
- [18] Griffith AA. The phenomena of rupture and flow in solids. Philos Trans R Soc Lond Ser A Containing papers of a mathematical or physical character 1921;221:163–98.
- [19] Mukherjee B, Dillard DA, Moore RB, Batra RC. Debonding of confined elastomeric layer using cohesive zone model. Int J Adhes Adhes 2016;66:114–27.
- [20] Slobbe AT. Propagation and band width of smeared cracks. Enschede, The Netherlands: Delft University of Technology; 2015.
- [21] Belytschko T, Fish J, Engelmann BE. A finite element with embedded localization zones. Comput Methods Appl Mech Eng 1988;70(1):59–89.
 [22] Stolarska M, Chopp DL, Moes N, Belytschko T. Modelling crack growth by
- [22] Stolarska M, Chopp DL, Moes N, Belytschko T. Modelling crack growth by level sets in the extended finite element method. Int J Numer Methods Eng 2001;51(8):943–60.
- [23] Benvenuti E. Mesh size objective XFEM for regularized continuous discontinuous transition. Finite Elem Anal Des 2011;47(12):1326–36.
- [24] Alfaiate J, Wells GN, Sluys LJ. On the use of embedded discontinuity elements with crack path continuity for mode-i and mixed-mode fracture. Eng Fract Mech 2002;69(6):661–86.
- [25] Jirasek M. Comparative study on finite elements with embedded discontinuities. Comput Methods Appl Mech Eng 2000;188(1):307–30.
- [26] Oliver J, Huespe AE. Continuum approach to material failure in strong discontinuity settings. Comput Methods Appl Mech Eng 2004;193(30):3195–220.

- [27] Oliver J, Huespe AE, Dias IF. Strain localization, strong discontinuities and material fracture: matches and mismatches. Comput Methods Appl Mech Eng 2012;241–244:323–36.
- [28] Moes N, Belytschko T. Extended finite element method for cohesive crack growth. Eng Fract Mech 2002;69(7):813–33.
- [29] Wells GN, Sluys LJ. A new method for modelling cohesive cracks using finite elements. Int J Numer Methods Eng 2001;50(12):2667–82.
- [30] Mosler J, Meschke G. Embedded crack vs. smeared crack models: a comparison of elementwise discontinuous crack path approaches with emphasis on mesh bias. Comput Methods Appl Mech Eng 2004;193(30):3351–75.
- [31] Hattori G, Rojas-Díaz R, Sáez A, Sukumar N, García-Sánchez F. New anisotropic crack-tip enrichment functions for the extended finite element method. Comput Mech 2012;50(5):591–601.
- [32] Shabir Z, Van der Giessen E, Duarte C, Simone A. The role of cohesive properties on intergranular crack propagation in brittle polycrystals. Model Simul Mater Sci Eng 2011;19(3):035006.
- [33] Ren W, Yang Z, Sharma R, Zhang C, Withers PJ. Two-dimensional x-ray ct image based meso-scale fracture modelling of concrete. Eng Fract Mech 2015;133:24–39.
- [34] Huang Y, Yan D, Yang Z, Liu G. 2D and 3D homogenization and fracture analysis of concrete based on in-situx-ray computed tomography images and monte carlo simulations. Eng Fract Mech 2016;163:37–54.
- [35] Huang Y, Yang Z, Ren W, Liu G, Zhang C. 3D meso-scale fracture modelling and validation of concrete based on in-situx-ray computed tomography images using damage plasticity model. Int J Solids Struct 2015;67:340–52.
- [36] Hendriks MA, Barros H, Faria R, Ferreira C, Rots JG. Sequentially linear versus nonlinear analysis of RC structures. Eng Comput 2013;30(6):792–801.
- [37] Zimmermann T, Jirasek M. Rotating crack model with transition to scalar damage. J Eng Mech 1998;124(3):277–84.
- [38] Rots JG, Blaauwendraad J. Crack models for concrete, discrete or smeared? fixed, multi-directional or rotating? HERON 1989;34(1).
- [39] Pineda EJ, Aeronautics USN, Administration S, Center NGR. Implementation of a smeared crack band model in a micromechanics framework. Technical Report; 2012. 217603;NASA/TM 2012–217603 National Aeronautics and Space Administration, Glenn Research Center, 2012.
- [40] Munjiza A. The combined finite-discrete element method. Wiley Online Library; 2004. ISBN 978-0-470-84199-0.
- [41] Slobbe AT, Hendriks MAN, Rots JG. Systematic assessment of directional mesh bias with periodic boundary conditions: applied to the crack band model. Eng Fract Mech 2013;109:186. doi:10.1016/j.engfracmech.2013.06.005.
- [42] Zimmermann T, Jirasek M. Analysis of rotating crack model. J Eng Mech 1998;124(8):842–51.
- [43] Rots J, Nauta P, Kuster G, Blaauwendraad J. Smeared crack approach and fracture localization in concrete. HERON, 30 (1), 1985 1985.
- [44] Rots J.G. Computational modeling of concrete fracture, Ph.D. thesis, Technische Hogeschool Delft, 1988.
- [45] Slobbe AT, Hendriks MAN, Rots JG. Sequentially linear analysis of shear critical reinforced concrete beams without shear reinforcement. Finite Elem Anal Des 2012;50:108–24.
- [46] Cook AC, Vel SS, Gerbi C, Johnson SE. Computational analysis of nonlinear creep of polyphase aggregates: influence of phase morphology. J Geophys Res: Solid Earth 2014;119(9):6877–906. doi:10.1002/2014JB011197.
- [47] Vel SS, Cook AC, Johnson SE, Gerbi C. Computational homogenization and micromechanical analysis of textured polycrystalline materials. Comput Methods Appl Mech Eng 2016;310:749–79.
- [48] Maynard P. Drawing distinctions: the varieties of graphic expression. Cornell University Press; 2005.
- [49] Oliver J. A consistent characteristic length for smeared cracking models. Int J Numer Methods Eng 1989;28(2):461–74.
- [50] Jirasek M, Bauer M. Numerical aspects of the crack band approach. Comput Struct 2012;110–111:60.
- [51] Govindjee S, Kay GJ, Simo JC. Anisotropic modelling and numerical simulation of brittle damage in concrete. Int J Numer Methods Eng 1995;38(21):3611–33.
- [52] Rots J, Nauta P, Kusters G. Variable reduction factor for the shear stiffness of cracked concrete. Technical Report.. Delft; 1984.
- [53] Hughes TJ. The finite element method: linear static and dynamic finite element analysis. Courier Corporation; 2012.
- [54] Nooru-Mohamed MB. Mixed-mode fracture of concrete: an experimental approach. TU Delft, Delft University of Technology; 1992.
- [55] Hordijk DA. Local approach to fatigue of concrete. TU Delft, Delft University of Technology: 1991.
- [56] Hordijk DA. Tensile and tensile fatigue behaviour of concrete; experiments, modelling and analyses. HERON 1992;37(1).
- [57] Salem JA, Li Z, Bradt RC. Thermal expansion and elastic anisotropy in single crystal Al2O3 and SIC reinforcements. Technical Report; 1994. 106516;NASA/TM 1994–106516 National Aeronautics and Space Administration, 1994.
- [58] AZoM. Sapphire single crystal alumina. 2016. URL http://www.azom.com/properties.aspx?ArticleID=1721, (Accessed September, 2016).
- [59] Seidel J, Claussen N, Rödel J. Reliability of alumina ceramics: effect of grain size. J Eur Ceram Soc 1995;15(5):395–404.
- [60] Zavattieri P, Espinosa H. Grain level analysis of crack initiation and propagation in brittle materials. Acta Mater 2001;49(20):4291–311.